MECHANICAL PROPERTIES OF CATHODE MATERIALS FOR LITHIUM ION BATTERIES

J.C. Stallard[1], L. Wheatcroft[2], S.G. Booth[2], R. Boston[2]
S.A. Corr[2], M.F.L De Volder[1], B.J. Inkson[2], N.A. Fleck[1]*

[1]Department of Engineering, University of Cambridge. Trumpington St., CB2 1PZ, UK.
[2]Department of Materials Science and Engineering, University of Sheffield, Mappin St., S1 3JD, UK.
*Corresponding Author: naf1@eng.cam.ac.uk

Abstract

Mechano-chemical degradation processes such as the fracture of cathode particles play a major role in limiting the service life of advanced lithium ion batteries (LIBs). In order to help alleviate degradation of battery performance, it is necessary to measure the relationship between the degradation of mechanical properties of cathodes and their concomitant degradation of electrochemical performance. In this review, measurements of the mechanical properties of LIB cathode materials are summarised from the literature, along with the range of experimental methods used in their determination. Dimensional changes that accompany charge and discharge are compared for active materials of olivine, spinel and layered atomic structures. The sensitivity of indentation hardness, Young's modulus and fracture strength to grain size, porosity, state of charge and charge/discharge history are critically reviewed, and are discussed with reference to the behaviour of conventional, electrically inactive solids. This approach allows for the identification of microstructural properties that dictate the mechanical properties of LIB cathode materials.

Keywords: Li-ion batteries, Cathode, active materials, mechanical properties, fracture.

1.   Introduction

The discovery of stable transition metal oxides for the repeated insertion and removal of lithium ions [1]–[3] has allowed for the widespread adoption of lithium-ion battery cathode materials in consumer electronics, such as cellular telephones and portable computers [4]. Lithium-ion batteries are also the dominant energy storage technology used in electric vehicles [5]. An increase in their specific energy density, power output and service life are required to further their uptake in the automotive sector and elsewhere [6], [7]. Increases in cell capacity rely upon the development of new active materials and electrode architectures [8]. To assist these efforts, a greater understanding of the relationship between mechanical properties, cathode performance and cathode degradation is required [4].

This review provides an overview of the mechanical properties of cathode active materials, and explores how they are modified by charging and by the application of repeated charge/discharge cycles. The measured mechanical properties of cathode materials are summarised, along with the experimental methods used in their determination. Correlations between the measured values of modulus, hardness, and fracture strength of cathode materials and their microstructures are identified and compared with those of electrically inactive ceramics. Recent experimental studies that document the sensitivity of mechanical properties to electrolyte immersion, state of charge and the number of charge/discharge cycles are also reviewed.

1.1.   The structure of a lithium ion cell

The essential components of a lithium ion cell are sketched in Figure 1. During discharge of the cell, the oxidation of Li atoms to positively charged lithium ions Li^+ and

electrons occurs at the anode. The Li^+ ions migrate from the anode to the cathode through the electrolyte, and for charge balance the electrons flow from the current collector of the anode via an external electrical circuit. The electrodes are insulated against electron flow within the cell by a separator membrane that is permeable to lithium ions [9]. The Li^+ ions diffuse into the active cathode material and remain in the ionic state. Electrons flow from the external circuit to the cathode and take part in a reduction reaction involving a transition metallic oxide [10], for example Co^{4+} to Co^{3+}, Ni^{4+} to Ni^{3+}, Mn^{4+} to Mn^{3+}, or Fe^{3+} to Fe^{2+}. When the cell is charged, the above processes are reversed: oxidation and reduction reactions occur at the cathode and the anode respectively, lithium ions migrate through the electrolyte from the cathode to the anode, and electrons flow from the cathode to the anode via their current collectors and an external circuit.

1.2.   Classes of cathode materials used in lithium ion cells

There exist an increasing number of transition metal oxides, with crystal structures that allow for the intercalation of lithium ions during cell discharge, and consequently have potential for use as the cathode of a LIB. The cathode materials that have received the greatest research and commercialisation attention to date fall into three classes, as illustrated in Figure 2(a-c) and as described below:

(a) *Olivine crystal structures/polyanion oxides*. An example is lithium iron phosphate (LFP) of composition $LiFePO_4$, for which the crystal structure is sketched in Figure 2(a). Oxygen atoms form a hexagonal close-packed lattice. Tetrahedral voids within the lattice are occupied by phosphate anions, and octahedral holes by iron and lithium cations. The voids occupied by lithium cations form continuous, parallel channels throughout the lattice [3]. The equilibrium diagram reveals that two distinct phases exist, $LiFePO_4$ and $FePO_4$,

however, the Li can also exist as a metastable solid solution of intermediate composition when it is inserted or extracted rapidly [11].

(b) *Layered oxides* comprise stacked layers of metal oxide compounds. Write a subscript x for the degree of lithiation. Then, these oxides include lithium cobalt oxide (LCO) of composition Li_xCoO_2, nickel cobalt aluminium (NCA) of composition $Li_xNi_yCo_zAl_{(1-y-z)}O_2$ and nickel manganese cobalt $Li_xNi_yMn_zCo_{(1-y-z)}O_2$ (NMC), as illustrated in Figure 2(b). Each metal oxide layer has two planes of oxygen atoms, between which transition metal atoms occupy interstitial holes. Lithium ions intercalate the gaps between the metal oxide compound layers, and form a one-atom thick lithium layer. Transport of lithium ions occurs within each lithium layer, giving rise to 2-dimensional diffusion [12]. The mobility of lithium ions within layered cathode active materials varies with their state of charge [13], [14].

(c) *Spinel oxides:* These include lithium manganese oxide spinel (LMO) of composition $Li_xMn_2O_4$ (LMO), in which the manganese atoms sit at the centre of octahedral voids within a lattice of oxygen atoms. Lithium ions migrate along paths of tetrahedral and octahedral voids and give rise to 3-dimensional diffusion [15]. Transition metal atoms such as Ni can partially replace the Mn, for example $Li_xNi_{0.5}Mn_{1.5}O_4$, to form a so-called 'ordered' spinel. Alternatively, if the transition metal atoms are randomly distributed within the lattice, a spinel is termed 'disordered'. The electrochemical properties of the spinel active materials are sensitive to the degree of ordering within the lattice [16]–[18].

A variety of cathode particle shapes exist for all 3 classes, and examples are sketched in Figure 2(d-g). Commonly, NMC cathodes comprise secondary particles of diameter 5-20 μm, as sketched in Figure 2(d). Each secondary particle is a polycrystal, and comprises grains of dimension 0.1 μm to 2 μm [19], commonly termed 'primary particles'. LCO, NMC and LFP

cathodes may also comprise equiaxed micron scale single crystals, see Figure 2(e). Alternatively, the single crystal particles can be (f) plate-shaped [20], or (g) nano-sized [21]. The power capacity of cathodes may benefit from smaller length scales over which ionic diffusion occurs in cycling, and the increased area of interface between particle and electrolyte over which ions migrate in charge and discharge.

Ideally, a battery has both a high power density and a high energy density. The measured specific power and specific energy for a wide range of LIB cathode materials [11], [19]–[29] are plotted in Figure 3(a), in what is commonly termed a Ragone plot. Here, the specific power and specific energy of the cathodes are the average power and energy measured during discharge, normalised by the mass of the cathode active material. In these charts, the upper limit to the specific energy is governed by the voltage at which the cathode active material undergoes lithiation, and by the capacity for lithiation [10]. Limitations on electrical and ionic transport within the cell lead to the limit in specific power [30].

The influence of LFP cathode particle architecture upon specific power is explored in Figure 3(b). The data are taken from the literature for LFP cathodes and are grouped according to cathode particle dimensions, shape, and presence or absence of a coating [11], [20]–[22], [27]–[29]. Interconnected porosity provides paths for electrolyte infiltration [22], and thin, flat and small particles enable an increased surface area per unit mass [20], [21]. For a given specific energy, the specific power varies by up to two orders of magnitude. The influence of particle size upon specific power is evaluated by plotting specific power versus particle dimension for all values of specific energy below 350 Wh kg^{-1} where the specific power approaches its largest value, see Figure 3(c). For any fixed shape of particle, the specific surface area in contact with electrolyte varies with the reciprocal of particle dimension: for

this reason contours of negative unit slope are included in Figure 3(c). If the specific power provided by the LFP cathodes is dictated by the specific surface area of the cathode particles, then a single line of slope -1 would be expected for the data of Figure 3(b). In fact, the specific power varies by a factor of x50 for a given particle size, implying that specific power is influenced by other features such as conductivity of the porous cathode composite [31], cathode porosity, and the tortuosity of the electrolyte-filled pore network [32]. And now a word of caution: a cathode of high porosity contains a significant mass of electrolyte and has an increased volume. Consequently, the power per unit mass and power per unit volume of the electrolyte-filled cathode are significantly less than that for the cathode active material alone [33]. This practical limitation is not evident in the Ragone plots of Figure 3, where measurements of specific power and specific energy have been normalised by the mass of the cathode active materials alone.

1.3. Dimensional changes of active material atomic structures during charge and discharge

The lithiation (or delithiation) of the active cathode materials leads to a distortion and dilation of their atomic lattices. Atomic lattice dimensions and active material phase proportions are measured by X-ray diffraction (XRD) experiments [34]. In-operando XRD cells [35] facilitate continuous monitoring of the cathode active material atomic structure and dimensions during charge and discharge. Most studies focus on delithiation from an initial state of full lithiation, $x = 1$.

Data for the normalised lattice constants a/a_0 and c/c_0 obtained from experiments for the first cell charge and reported in the literature [36]–[42] are plotted in Figure 4(a) and 4(b), respectively, as a function of the degree of lithiation, x in Li$_x$MO$_b$. Here $x = 1$

corresponds to a state of full lithiation for the active material for both layered and spinel classes of cathode materials, and a_0, b_0 and c_0 are lattice constants in the fully lithiated state [36], [39]. The symmetries possessed by the spinel and layered oxide crystal structures imply that $b/b_0 = a/a_0$. (Data are not shown for LFP since two distinct phases exist in equilibrium, $LiFePO_4$ and $FePO_4$, and the relative proportion of these phases changes with x.) The changes in unit cell dimensions upon delithiation (that is, upon battery charging) have both volumetric and distortional components. To describe these changes, the normalised unit cell parameter c/c_0 measured in-situ during cell charge is plotted against $(ab)/(a_0b_0)$ in Figure 4(c). A line of constant volume is included in Figure 4(c) to show purely distortional straining, along with a line of isotropic shrinkage (no distortion).

First, consider the dimensional changes that occur within the atomic lattices of layered NMC oxides over the initial charge cycle of the cell [36], [37], [39]. NMC oxide lattices initially expand along their c direction; this is attributed to a loss of electrostatic shielding between the positively charged transition metal oxide layers as lithium atoms are removed [36]. Contraction in the a and b direcions also occur as the ionic radii of the transition metal atoms decrease with electron loss [40], keeping the unit cell volume approximately constant. As delithiation proceeds, such that the occupancy of lithium within the cathode becomes $x < 0.4$, nickel oxidation and shrinkage of the separation between the O^{2-} planes across each lithium layer lead to a decrease in the c lattice dimension [41]. The dimensional changes that occur in layered NMC cathodes over the charge cycle are sensitive to the chemical composition of the transition metal oxide layers [37] and also to the doping of other atoms alongside lithium in the vacancies between the transition metal oxide layers [43].

As LCO is delithiated, two phases coexist for $0.75 < x < 1.0$, and the unit cell volume initially increases [44], see Figure 4(c). A phase change subsequently occurs at a lithium occupancy of $x = 0.5$, as the unit cell transitions from a hexagonal to monoclinic atomic structure [45]. Consequently, the amount of Li extracted from these cathodes is limited to 50% to maintain the stability of the crystal structure [39].

Data for spinel lattices [16], [17] of composition $Li_x Mn_2 O_4$ are included in Figure 4. For these materials, isotropic shrinkage accompanies delithiation and three separate phases are formed as the degree of delithiation is reduced [16], which coexist for portions of the charge response. The greatest change in lattice dimension occur as the lattice transitions from one phase to the next; dimensional changes of each phase are small with decreasing x. The lithium occupancy x over which phase changes occur, and the dimensional changes that they impart, are sensitive to Ni doping [16]–[18], the degree of ordering within the spinel lattice [17], and spinel chemical composition [42]. Ni doping, combined with a disordered lattice structure (such that Ni and Mn are randomly distributed throughout the lattice), prevents the phase change from occurring until the lithium fraction x decreases below 0.13. For all lithium fractions above this value, the unit cell dimensions remain within 1% of their value in the fully lithiated state [17].

1.4.   Chemo-mechanical degradation in lithium ion cells

Experiments reveal that the charge capacity of lithium ion batteries decreases over successive charge/discharge cycles [46]. The rate of capacity loss depends upon operating conditions such as the range of voltage employed during operation, the rate of charge transfer imposed, and the cell temperature [46], [47]. The specific energy and power density of lithium ion cells, and the rate of capacity loss upon repetitive cycling are also sensitive to the active

material class and composition [48], the size and shape of the active material particles [49], [50], and electrolyte composition [51], [52]. The chemical and mechanical phenomena that lead to a loss in charge capacity, increase cell resistance and limit cell life include the following:

(i) the growth of passivating layers upon the surface of electrode particles in contact with the electrolyte [53];

(ii) the loss of active material to passivating layers or electrolyte; and

(iii) the growth of cracks within active material particles, which in turn promote mechanisms (i) and (ii) [54].

Calculations reported in the literature suggest that the stresses that arise within cathode particles during charge and discharge are sufficient to lead to their fracture [55]–[57]. In the case of polycrystalline secondary particles of layered active materials such as NMC, differential swelling between adjacent primary grains upon charging can give rise to intergranular cracking [9], as sketched in Figure 5; electrolyte may infiltrate along these intergranular cracks. Numerical simulations confirm that the magnitude of swelling-induced stresses depends upon the charging rate, particle size, particle shape, and ionic and electrical conductivity [58]–[60]. Polycrystalline active material particles may develop cracks both within and between their grains [8], [9], [61]. Numerical simulations suggest that the rate at which fracture proceeds is linked to the progressive loss of cathode particle toughness with changes in lithium occupancy [62]. Considerable interest exists in the design and development of active material particles and electrode architectures that are resistant to fracture during charge and discharge [63], [64].

2. The modulus, hardness and fracture strength of dry, as-manufactured cathode materials

The mechanical properties of cathode materials are commonly characterised by the Young's modulus E, indentation hardness H and fracture strength σ_F in the fully lithiated but dry state prior to immersion in the liquid electrolyte [65]–[76]. In this section, the test methods used to measure the modulus, hardness and fracture strength of cathode materials are described alongside the results from experiments published in the literature. The properties are discussed in the context of the mechanical behaviour of other conventional, brittle solids.

2.1. Indentation measurement of hardness and modulus

The Young's modulus and hardness of cathode materials has been measured in several studies with a sharp 3-sided pyramidal indenter, as sketched in Figure 6(a) [65]–[77]. In such indentation tests, an indentation tip is lowered onto the surface of the test specimen and subjected to a vertical load P_I. The indentation load is then removed, and the tip withdrawn from the sample surface. This gives rise to a permanent indentation of the sample surface, of similar shape to that of the indenter tip. The indentation hardness H is related to the indentation load P_I and projected area of the indentation mark A_P, according to

$$H = \frac{P_I}{A_P}.$$

(1)

For the case where plastic flow occurs beneath the indenter, the hardness is directly related to the yield strength σ_Y, such that $H \approx 3\sigma_Y$; the indentation hardness is only weakly dependent upon the tip geometry [78].

The force versus displacement relation in a typical indentation test on an elasto-plastic solid is sketched in Figure 6(b). Unloading from the maximum load is an elastic event, and so the Young's modulus of the solid E is obtained directly from the unloading stiffness S and the contact area A_P between sample and indenter [79], [80]. The usual method is to take into account the Young's modulus E_I of the indenter material in order to obtain a reduced modulus E_R where

$$E_R = \frac{(1 - v^2)}{E} + \frac{(1 - v_I^2)}{E_I} \tag{2}$$

in terms of the Poisson ration v for the solid and v_I for the indenter. The unloading slope S depends upon E_R and A_P according to $S = 2E_R(A_P/\pi)^{1/2}$ [81].

Commonly, the 3-sided diamond indenter has a tip radius R on the order of 1 μm. Consequently, indentation tests can measure the properties of small volumes of material, such as cathode secondary particles, or an individual grain of a large-grained polycrystalline sample. To measure the hardness and modulus of cathode secondary particles, a cathode may be set in resin and the cross-section of the particle is exposed by grinding and polishing of the surface, as sketched in Figure 6(c). Alternatively, macroscopic polycrystalline samples of cathode materials may be manufactured by sintering, and prepared for indentation testing by grinding and polishing of the surface [75], see Figure 6(d).

The hardness and Young's modulus of a range of cathode materials are plotted in Figure 7, from [65]–[76]. The hardness varies from 6 GPa to 18 GPa, while the Young's modulus varies from 80 GPa to 200 GPa. Engineering glasses and ceramics have comparable values of hardness and modulus [82], [83], as also shown in Figure 7. All fail in an elastic-

brittle manner upon the application of a tensile stress: their tensile fracture strength is dictated by fast fracture from pre-existing flaws [83].

Size effects in indentation testing are reported in numerous investigations of ceramic and metallic materials. They may arise from a variety of factors associated with experiment [84], [85]. Specimen surfaces may be work-hardened by polishing [86], or form oxide layers [87]. Size effects may also arise due to the rounding of an indentation tip close to its apex, as the indentation area deduced from the indentation depth with a calibration such as that in equation (3) may not accurately predict the indentation area if its size is comparable to the rounded apex [88].

The microstructural mechanisms associated with yielding of a polycrystalline ceramic during indentation testing have been widely studied [89]–[93], and are sketched in Figure 8. Three distinct deformation mechanisms exist, as follows.

Stage I: Dislocation-based plasticity. Initially, the size of an indent positioned in the mid-grain is much less than the grain size. In this regime, the hardness is dictated by dislocation-based plasticity within an individual grain.

Stage II: Initiation of intergranular fracture. The plastic zone expands with increasing indentation size, and grain boundaries crack near the indenter tip [89], [90].

Stage III: Activation of granular flow. Bulk flow of the fractured grains requires dilatation [94], [95] into a granular medium at its critical state, reminiscent of the 'plastic' response of an over-consolidated soil [93], [96]. The hardness scales with the cohesive strength of the granular medium.

The deformation mechanisms that dictate hardness in each of the three stages described above may activate in sequence as the size of the indentation increases relative to the dimensions of the grains. For indentation experiments performed with Berkovich indentation tips, the indentation area A_P is related to the indentation depth d_I as

$$A_P = 24.5 d_I^2 \qquad (3)$$

in the absence of pile-up [88].

The Young's modulus and indentation hardness measured for polycrystalline samples of the layered cathode materials $LiNi_{0.5}Mn_{0.3}Co_{0.2}O_2$ (NMC532), $LiNi_{1/3}Mn_{1/3}Co_{1/3}O_2$ (NMC333) and LCO are plotted as a function of contact size $A_P^{1/2}$, as deduced from the measured indentation depth according to equation (3) in Figure 9(a) and 9(b) respectively [65], [73]–[76], [97]. The grain size within the secondary particles lies between 0.1 μm and 1 μm, whereas the hot-pressed pellets are of larger grain size between 3 μm and 100 μm.

As indentation depth increases, different mechanisms of deformation may give rise to size effects. In stage I, hardness derives from the inelastic strains due to dislocation motion and twinning within the atomic lattice [92], [98]. For indentations in this range, an increase in hardness with decreasing indentation size without any similar increase in elastic modulus is taken as evidence of similar strain gradient effects to those measured in many other crystalline materials where plasticity is due to dislocation glide [99], [100]. If an indentation is sufficiently small in dimension, a higher density of geometrically necessary dislocations exist to realise the plastic strain imposed by the indenter [99]; this higher dislocation density then gives rise to an increased hardness [100], but leaves the modulus unaltered. Predictions for

the variation of indentation hardness with indentation load based upon this premise have been successful in capturing experimental trends observed in other crystalline solids [100].

In stage II, intergranular fracture around the indenter initiates. Finally, the hardness in stage III is set by the granular flow of the solid, as a result of diffuse grain boundary cracking and the associated dilation [92], [94], [95]. To assess the relative influence of plasticity and additional compliance associated with cracking along grain boundaries, measured values of modulus and hardness obtained from indentation tests are plotted against the size of the indentation $A_P^{1/2}$ normalised by the grain size d, in Figures 9(c) and 9(d), respectively. This choice of normalisation brings the data together and reveals the origin of the size effect: it is the grain size that sets the material length scale. The decrease of both modulus and hardness with increasing $A_P^{1/2}/d$ for $\left(A_P^{1/2}/d\right) > 0.1$ is associated with fragmentation by grain boundary fracture [101], [102], whereas for indents of size $\left(A_P^{1/2}/d\right) < 0.1$, the Young's modulus is relatively insensitive to a variation in $A_P^{1/2}/d$. In cathode materials of large grain size, a radial pattern of fractures can initiate beneath the indentation tip within the mid-grain without initially progressing to the nearest grain boundary [65], [103]. This forms a well-defined pattern of fractures that allows for an estimation of the fracture toughness [104], [105]. The presence of cracks reduces the macroscopic, effective modulus of the solid and thereby reduces the unloading stiffness of the indentation test.

2.2.   Measurement and origin of fracture strength

Measurements of the tensile fracture strength of polycrystalline secondary particles and the origin of the fracture strength are now discussed. Experiments are performed on the individual secondary particles that comprise cathodes, of typical diameter 10 μm, and on

macroscopic samples such as sintered cylindrical pellets. The tensile fracture strength σ_F of brittle particles may be determined by measuring the compressive load at fracture P_C between two platens in a 'Brazil-nut test' [106], [107], see Figure 10(a). A tensile stress in the transverse direction is induced when a spherical sample is subjected to a compressive diametral load [108]. The tensile strength at fracture σ_F is approximately related to the compressive load at failure P_C and particle diameter d_P, according to [107], [109]:

$$\sigma_F = 2.8 \frac{P_C}{\pi d_P^2}. \qquad (3)$$

Bi-axial flexure tests on cylindrical specimens, as sketched in Figure 10(b), have been used to determine the tensile fracture strength of macroscopic cylindrical active material samples [110]. In these tests, a cylindrical disc-shaped sample is supported around its edge by a ring. The sample is then loaded centrally through a second, smaller ring. The resulting tensile stress reaches a maximum in the centre of the lower face. The fracture strength is deduced from the measured load at fracture P_F and the sample geometry via an elastic calculation [111].

Measurements of the fracture strength of polycrystalline samples of $LiNi_{1/3}Mn_{1/3}Co_{1/3}O_2$ reported in the literature [106], [110] are plotted in Figure 10(c) against the measured grain size for each sample [112]. For data obtained from tests on sintered pellets, sample porosity is written next to the data as a percentage. Note that the tensile strengths are an order of magnitude or more below the uniaxial yield strength $\sigma_Y \approx H/3$ for all of the layered transition metal oxides reported in the literature and summarised in Figure 7.

The tensile strength of brittle materials, such as cathode secondary particles and the associated polycrystalline pellets, are dictated by the propagation of pre-existing flaws within them. Define the fracture strength σ_F as the maximum tensile stress that a specimen of brittle material may withstand without the propagation of a pre-existing sharp flaw within it. One such flaw of length $2a$ oriented perpendicular to an applied tensile stress σ is sketched in Figure 11(a). The tensile fracture strength σ_F is related to the fracture toughness K_{IC} and flaw length a, according to $K_{IC} = \sigma_F\sqrt{\pi a}$. Consequently, the fracture strength σ_F increases with decreasing flaw size. If all flaws within a specimen are sufficiently small, the uniaxial yield strength $\sigma_Y \approx H/3$ may be less than their fracture strength σ_F. The result is ductile failure, as occurs in many metals.

Polycrystalline cathode materials may contain flaws within an individual grain, or within a grain boundary, as sketched in Figure 11(b). In both cases, the length of such pre-existing flaws is on the order of the grain size [113], [114]. Upon relating the characteristic flaw dimension a to the grain size d according to $a = d/2$, and taking the fracture strength $\sigma_F = K_{IC}/\sqrt{\pi a}$, predictions for fracture strength are obtained over the range of grain sizes reported in the literature, and plotted as contours of constant K_{IC} in Figure 8(c). With the exception of samples with porosity exceeding 11%, the measured fracture strength of NMC sintered pellets increases with decreasing grain size, as expected from the above considerations. A comparison of the predictions with the experimental measurements implies a fracture toughness K_{IC} between 0.05 MPa m$^{1/2}$ and 0.3 MPa m$^{1/2}$ for polycrystalline samples of fully-lithiated, layered NMC333, see Figure 8(c). This low value of toughness for a polycrystalline ceramic is typically associated with intergranular fracture [110]. For comparison, the fracture toughness measured by indentation within large single grains of

LiCoO$_2$ lies between 0.2 MPa m$^{1/2}$ and 6.5 MPa m$^{1/2}$, and varies with the orientation of the indentation relative to that of the layered atomic structure within the grain [65]. The fact that the intergranular toughness is much below the transgranular toughness explains the observation that intergranular fracture is observed upon cell charging [9].

3. Effects of electrolyte immersion, state of charge and charge/discharge cycles upon mechanical properties

The effects of electrolyte immersion and cell cycling upon the mechanical properties of cathode materials are directly relevant to cell design. In this section, data from the literature are assembled to assess the origin and degree of degradation of mechanical properties in cell operation.

3.1. Effect of electrolyte immersion on mechanical properties

The Young's modulus, hardness and fracture strength of as-manufactured LiNi$_{0.5}$Mn$_{0.3}$Co$_{0.2}$O$_2$ polycrystalline pellets and secondary particles have been measured by indentation testing in the dry state and also during immersion in a liquid electrolyte, 1 M LiPF$_6$ in polypropylene carbonate [73]. The measured modulus and hardness in the dry state and in the immersed state are compared in Figure 12(a). Both modulus and hardness have a low sensitivity to immersion in an electrolyte. Additional measurements of the fracture strength of NMC333 secondary particles with single particle compression tests have been obtained before and after immersion in an electrolyte of 1 M LiPF$_6$ in ethylene carbonate for 48 hours, rinsing in dimethyl carbonate and suspension in N-methyl-2-pyrrolidone at 80°C for 30 minutes, and drying: the fracture strength is similarly unchanged by immersion [106]. It is

concluded that immersion of NMC cathode materials in liquid electrolytes gives only minimal degradation in their mechanical properties.

3.2. Dependence of modulus and hardness upon the degree of lithiation

The effect of delithiation upon the modulus, hardness and fracture of cathode materials is now addressed. But first, a word of caution. Sometimes in mechanical studies, high values of upper cut off voltage (UCV) are chosen in order to exaggerate the degree of cracking, which is not representative of behaviour at a lower value of UCV. For example, for NMC811, a UCV of 4.8 V may be used, whereas the maximum voltage in practical cycling is 4.2 V to 4.3 V [115].

The Young's modulus E and hardness H of layered cathode materials and spinel lithium manganese oxide are plotted in Figures 12(b) and (c) as a function of the degree of lithiation within the cathode x during the first cell charge [68], [72], [97], [116]. At $x = 1$ the cathode is fully lithiated; as the cell is charged x decreases towards $x = 0$, which corresponds to complete delithiation. The modulus E and hardness H of spinel LMO are almost insensitive to the occupancy x. In contrast, the measured modulus and hardness of the layered cathode materials NMC532 and LCO both decrease with decreasing lithium occupancy, and this can be traced to the generation of intergranular cracks upon delithiation [9], [61]. Whilst data for the layered NMC532 cathode material obtained from measurements of secondary particles show a monotonic, progressive decrease in modulus and hardness with decreasing x, measurements of the thin film polycrystalline LCO cathode with grain size of approximately 80 μm reveal an abrupt initial decrease from $x = 1$. The indentation size is much below the grain dimension [97], and the dimensional change of the LCO lattice upon delithiation is initially minor [44], see Figure 4. Note that the delithiation of LCO initially leads to the

formation of a distinct second hexagonal phase [44] which coexists for x in the range $0.75 <$ $x < 1.0$. Consequently, the observed initial softening may be due to the formation of a new phase during initial discharge, rather than from microcracking due to changes in the lattice dimensions [97]. Write E_0 and H_0 as the values of modulus and hardness in the initial fully lithiated state. The plot of H/H_0 versus E/E_0 in Figure 12(d) reveals that the fractional degradations in modulus and hardness are similarly affected by the cell charge.

3.3.   Influence of charge/discharge cycles upon modulus, hardness and fracture strength

It is emphasised that the experimental results discussed in this section are sensitive to the details of the electrochemical tests, such as the upper cut-off voltage, if a cathode is part of a full cell or half cell, and the composition of the electrolyte. Furthermore, the particle architecture is also important: for example, single crystal cathode particles can avoid cracking from differential straining between grains within a polycrystal. Results obtained from the study of polycrystalline layered cathode particles cannot be extrapolated to all cathode materials or particle architectures.

Initially, consider the effect of the first delithiation followed by the first relithiation upon the fracture strength of polycrystalline cathode particles that comprise grains of layered NMC333. The measured fracture strength of NMC333 cathode particles is plotted against lithium occupancy x in Figure 13(a) in the as-manufactured, lithiated state, after the first delithiation, and then after subsequent relithiation [106]. The measurements reveal that the drop in fracture strength due to delithiation is partially recovered upon subsequent relithiation. Nonetheless, the fracture strength remains much below that measured for the

pristine state. This is attributed to the growth of microcracks between the primary grains upon delithiation [9], [117].

After a single cycle, secondary particles possess an average fracture strength only 44% of that measured for pristine particles [106], see Figure 13(a). Recall that the fracture strength σ_F varies with flaw size a and fracture toughness K_{IC} according to $\sigma_F = K_{IC}\sqrt{\pi a}$. If the fracture toughness of grain boundaries remains constant (and that the fracture strength of cathode particles remains constant, then the flaw size a within the particles increases by a factor of about 5 over the first cycle. The conclusion that cracks within secondary particles advance upon delithiation is consistent with the measured increase in ionic transport upon charging, also attributed to the cracking which increases the particle surface area over which ionic transport occurs [117].

The degradation of Young's modulus and hardness of cathode materials, as a function of the number of applied charge/discharge cycles, are assembled in Figure 13(b) and (c) from [70], [74]. The greatest changes in mechanical properties occur in the first cycle [106], [116], [117]; where data for the first cycle are absent, dotted lines are used to connect the data. For thin film spinel LMO cathodes, the decrease in hardness and Young's modulus with cycling increases with increasing charging current (C-rate). The measured decrease in modulus upon repetitive cycling correlates with the accompanying decrease in hardness, see the plot of H/H_0 versus E/E_0 in Figure 12(d).

Now consider the micromechanical origin of the decrease in hardness and modulus upon repeated cycling. The hardness and modulus of a range of polycrystalline brittle materials have been measured as a function of their porosity [118]–[120], revealing that hardness, modulus and fracture strength all decrease with increasing porosity. High-

resolution computed tomography studies [121] reported in the literature revealed that the porosity of a Li$_x$Ni$_{0.8}$Mn$_{0.1}$Co$_{0.1}$O$_2$ secondary particle increased from 0.14 to 0.19 over 5 cycles. The sensitivity of hardness and modulus to porosity f_P are often successfully described by empirical relationships of the form $H = H_0 e^{-\alpha f_P}$ and $E = E_0 e^{-\beta f_P}$, where H_0 and E_0 are values of modulus and hardness evaluated for $f_P = 0$, and values of the constants α and β are sensitive to microstructural features such as the intergranular strength and the degree of mechanical interlocking between grains [118], [122]. The continued decrease in hardness and modulus with increasing cycle number, see Figure 12(b) and 12(c), suggests that the porosity of the secondary particles continues to increase with additional cycling.

3.4.   Strategies to limit mechanical degradation of cathode material

Cathode particle fracture may arise from non-uniform swelling within each particle due to non-uniform lithium occupancy. This is promoted by a fast charge and gives rise to the so-called "electrochemical shock" [58]. Fracture can also arise from the anisotropic straining of neighbouring grains of differing lattice orientation, recall Figure 5. A number of approaches have been developed to avoid and reduce the mechanical degradation of cathode particles during electrochemical cycling [123]–[126]; a brief discussion of some of these methods is now provided.

(i)   Reduce the level of swelling strain over a charge/discharge cycle. In addition to restricting the voltage range in in operation to regions where only modest strains occur [127], the swelling strain within the cathode material atomic lattice can also be reduced by control of cathode composition [37] and by suitable doping [128], [129].

(ii)   Vary cathode composition within a secondary particle, either as a 'core-shell' particle architecture with distinct surface layer, or with a smooth variation in composition

from the particle core to exterior [130]. This strategy can decrease the tensile stress experienced at a cathode particle surface during delithiation, thus avoiding microcracking upon cell charge [131]–[133].

(iii) Decrease primary particle size in polycrystalline secondary particles to limit the size of flaws. Experiments have shown that this approach can lead to greater resistance to microcracking [134], [135].

(iv) Eliminate the elastic constraint between cathode particle grains. If stresses in cycling arise from differential straining between neighbouring primary particles, an alignment of lattice orientation from grain to grain decreases the level of induced tensile stress during cycling, and thereby reduces the possibility of intergranular fracture [136].

(v) Use of a single-crystal particle architecture to remove the mismatched stresses that form in polycrystals due to differential straining of anisotropic grains [137]–[139]. By definition, single crystals do not contain grain boundaries.

(vi) Decrease the length scale for Li ion diffusion, for example by decreasing the size of secondary particles [58].

4. Conclusions

Indentation measurements of NMC cathode materials reveal a sensitivity of modulus and hardness to the ratio of indentation size to grain size. The degradation of both properties with increasing indent size is explained in terms of an increasing degree of intergranular cracking. The tensile fracture strength of pristine cathode particles is more than an order of magnitude below their indentation hardness; their low tensile strength is ascribed to the presence of pre-existing intergranular cracks. Reported measurements of the tensile fracture

strength σ_F of NMC polycrystalline cathode particles and larger NMC polycrystalline pellets scale with their grain size d, according to $\sigma_F \propto d^{-1/2}$; this behaviour is typical of that for polycrystalline engineering ceramics: tensile failure initiates from flaws of characteristic dimension comparable to the grain size.

The lithiation and delithiation of layered, olivine and spinel cathode material alters the dimensions of their atomic lattices. In the case of spinels, this dimensional change is isotropic, whereas the change in unit cell dimension of layered cathode materials strain is highly anisotropic. This provides an explanation for why secondary particles of layered cathode materials suffer substantial grain boundary fragmentation upon their first charge. Intergranular cracking leads to a decrease in the modulus, hardness and fracture strength of the secondary particles, which continues to progress upon repetitive cycling. The fractional decrease in the cathode hardness and modulus due to cell charging and cycling correlate, revealing that microcracking degrades both properties in a similar manner.

The extent of microcracking can be controlled via a variety of different particle-based strategie, the relevance of which depends upon if fracture arises from non-uniform lithiation due to fast charging, or anisotropic swelling of primary grains. These strategies include limiting active material strains though control of the voltage or composition, decreasing the size of primary or secondary particles, and enhancing their ionic conductivity. If microcracking occurs due to anisotropic straining between adjacent primary grains, then microcracking is reduced by aligning neighbouring grains within a secondary particle or by use of single crystal cathode particles.

Acknowledgements:

References:

[1]   K. Mizushima, P. C. Jones, P. J. Wiseman, and J. B. Goodenough, "LixCoO2 (0<x<-1): A new cathode material for batteries of high energy density," *Mater. Res. Bull.*, vol. 15, no. 6, pp. 783–789, Jun. 1980.

[2]   M. M. Thackeray, W. I. F. David, P. G. Bruce, and J. B. Goodenough, "Lithium insertion into manganese spinels," *Mater. Res. Bull.*, vol. 18, no. 4, pp. 461–472, Apr. 1983.

[3]   A. K. Padhi, K. 5 Nanjundaswamy, and J. B. Goodenough, "Phospho-olivines as positive-electrode materials for rechargeable lithium batteries," *J. Electroanal. Chem*, vol. 144, no. 4, p. 16, 1997.

[4]   N.-S. Choi *et al.*, "Challenges facing lithium batteries and electrical double-layer capacitors," *Angew. Chemie - Int. Ed.*, vol. 51, no. 40, pp. 9994–10024, 2012.

[5]   S.-T. Myung *et al.*, "Nickel-Rich Layered Cathode Materials for Automotive Lithium-Ion Batteries: Achievements and Perspectives," *ACS Energy Lett.*, vol. 2, no. 1, pp. 196–223, 2017.

[6]   J. B. Goodenough and Y. Kim, "Challenges for rechargeable Li batteries," *Chem. Mater.*, vol. 22, no. 3, pp. 587–603, 2010.

[7]   M. M. Thackeray, C. Wolverton, and E. D. Isaacs, "Electrical energy storage for transportation - Approaching the limits of, and going beyond, lithium-ion batteries," *Energy Environ. Sci.*, vol. 5, no. 7, pp. 7854–7863, 2012.

[8]   P. Yan, J. Zheng, M. Gu, J. Xiao, J.-G. Zhang, and C.-M. Wang, "Intragranular cracking as a critical barrier for high-voltage usage of layer-structured cathode for lithium-ion batteries," *Nat. Commun.*, vol. 8, 2017.

[9]   D. J. Miller, C. Proff, J. G. Wen, D. P. Abraham, and J. Bareño, "Observation of microstructural evolution in li battery cathode oxide particles by in situ electron microscopy," *Adv. Energy Mater.*, vol. 3, no. 8, pp. 1098–1103, 2013.

[10]   A. Manthiram, "A reflection on lithium-ion battery cathode chemistry," *Nat. Commun.*, vol. 11, no. 1, 2020.

[11]   H. Liu *et al.*, "Capturing metastable structures during high-rate cycling of LiFePO$_4$ nanoparticle electrodes," *Science (80-.).*, vol. 344, no. 6191, 2014.

[12]   C. Fisher, S. M. S. Islam, C. A. J. Fisher, and M. Saiful Islam, "As featured in: Lithium and sodium battery cathode materials: computational insights into voltage, diffusion

and nanostructural properties," *Chem. Soc. Rev*, vol. 43, p. 185, 2014.

[13]   Y. Wei *et al.*, "Kinetics Tuning of Li-Ion Diffusion in Layered Li(Ni$_x$Mn$_y$Co$_z$)O$_2$," *J. Am. Chem. Soc.*, vol. 137, no. 26, pp. 8364–8367, Jul. 2015.

[14]   K. Märker, P. J. Reeves, C. Xu, K. J. Griffith, and C. P. Grey, "Evolution of Structure and Lithium Dynamics in LiNi$_{0.8}$Mn$_{0.1}$Co$_{0.1}$O$_2$ (NMC811) Cathodes during Electrochemical Cycling," *Chem. Mater.*, vol. 31, no. 7, pp. 2545–2554, 2019.

[15]   B. Xu and S. Meng, "Factors affecting Li mobility in spinel LiMn$_2$O$_4$-A first-principles study by GGA and GGA+U methods," *J. Power Sources*, vol. 195, no. 15, pp. 4971–4976, 2010.

[16]   Y. J. Lee, F. Wang, S. Mukerjee, J. McBreen, and C. P. Grey, "^{6}Li and ^{7}Li Magic-Angle Spinning Nuclear Magnetic Resonance and In Situ X-Ray Diffraction Studies of the Charging and Discharging of Li$_x$Mn$_x$O$_4$ at 4 V," *J. Electrochem. Soc.*, vol. 147, no. 3, p. 803, 2000.

[17]   J. Zheng *et al.*, "Enhanced Li$^+$ ion transport in LiNi$_{0.5}$Mn$_{1.5}$O$_4$ through control of site disorder," *Phys. Chem. Chem. Phys.*, vol. 14, no. 39, pp. 13515–13521, Oct. 2012.

[18]   W. Li, B. Song, and A. Manthiram, "High-voltage positive electrode materials for lithium-ion batteries," *Chemical Society Reviews*, vol. 46, no. 10. Royal Society of Chemistry, pp. 3006–3059, May 2017.

[19]   H.-J. Noh, S. Youn, C. S. Yoon, and Y.-K. Sun, "Comparison of the structural and electrochemical properties of layered Li[Ni$_x$Co$_y$Mn$_z$]O$_2$ (x = 1/3, 0.5, 0.6, 0.7, 0.8 and 0.85) cathode material for lithium-ion batteries," *J. Power Sources*, vol. 233, pp. 121–130, 2013.

[20]   Y. Zhao, L. Peng, B. Liu, and G. Yu, "Single-crystalline LiFePO$_4$ nanosheets for high-rate Li-ion batteries," *Nano Lett.*, vol. 14, no. 5, pp. 2849–2853, 2014.

[21]   B. Kang and G. Ceder, "Battery materials for ultrafast charging and discharging," *Nature*, vol. 458, no. 7235, pp. 190–193, 2009.

[22]   Y. Ren and P. G. Bruce, "Mesoporous LiFePO$_4$ as a cathode material for rechargeable lithium ion batteries," *Electrochem. commun.*, vol. 17, no. 1, pp. 60–62, 2012.

[23]   U.-H. Kim *et al.*, "Pushing the limit of layered transition metal oxide cathodes for high-energy density rechargeable Li ion batteries," *Energy Environ. Sci.*, vol. 11, no. 5, pp. 1271–1279, 2018.

[24]   Y. Shi *et al.*, "A high-performance solid-state synthesized LiVOPO$_4$ for lithium-ion batteries," *Electrochem. commun.*, vol. 105, 2019.

[25]   Y. Shin and A. Manthiram, "Influence of microstructure on the electrochemical performance of LiMn$_{2-y-z}$Li$_y$Ni$_z$O$_4$ spinel cathodes in rechargeable lithium batteries," *J. Power Sources*, vol. 126, no. 1–2, pp. 169–174, 2004.

[26]   C. Yin, H. Zhou, Z. Yang, and J. Li, "Synthesis and Electrochemical Properties of LiNi$_{0.5}$Mn$_{1.5}$O$_4$ for Li-Ion Batteries by the Metal-Organic Framework Method," *ACS Appl. Mater. Interfaces*, vol. 10, no. 16, pp. 13624–13634, 2018.

[27] Y. Wang, Y. Wang, E. Hosono, K. Wang, and H. Zhou, "The design of a LiFePO$_4$/carbon nanocomposite with a core-shell structure and its synthesis by an in situ polymerization restriction method," *Angew. Chemie - Int. Ed.*, vol. 47, no. 39, pp. 7461–7465, 2008.

[28] H. Huang, S.-C. Yin, and L. F. Nazar, "Approaching theoretical capacity of LiFePO$_4$ at room temperature at high rates," *Electrochem. Solid-State Lett.*, vol. 4, no. 10, 2001.

[29] L. Guo *et al.*, "Unlocking the energy capabilities of micron-sized LiFePO 4," *Nat. Commun.*, vol. 6, 2015.

[30] X. Ma *et al.*, "Hindering rollover failure of Li[Ni$_{0.5}$Mn$_{0.3}$Co$_{0.2}$]O$_2$/Graphite pouch cells during long-term cycling," *J. Electrochem. Soc.*, vol. 166, no. 4, pp. A711–A724, 2019.

[31] N. Nitta, F. Wu, J. T. Lee, and G. Yushin, "Li-ion battery materials: Present and future," *Mater. Today*, vol. 18, no. 5, pp. 252–264, 2015.

[32] N. Kang *et al.*, "Cathode porosity is a missing key parameter to optimize lithium-sulfur battery energy density," *Nat. Commun.*, vol. 10, no. 1, 2019.

[33] Y. Son *et al.*, "Reliable protocols for calculating the specific energy and energy density of Li-Ion batteries," *Mater. Today Energy*, vol. 21, p. 100838, Sep. 2021.

[34] S.-M. Bak, Z. Shadike, R. Lin, X. Yu, and X.-Q. Yang, "In situ/operando synchrotron-based X-ray techniques for lithium-ion battery research," *NPG Asia Mater.*, vol. 10, no. 7, pp. 563–580, 2018.

[35] O. J. Borkiewicz, B. Shyam, K. M. Wiaderek, C. Kurtz, P. J. Chupas, and K. W. Chapman, "The AMPIX electrochemical cell: A versatile apparatus for in situ X-ray scattering and spectroscopic measurements," *J. Appl. Crystallogr.*, vol. 45, no. 6, pp. 1261–1269, 2012.

[36] L. De Biasi, A. O. Kondrakov, H. Geßwein, T. Brezesinski, P. Hartmann, and J. Janek, "Between Scylla and Charybdis: Balancing among Structural Stability and Energy Density of Layered NCM Cathode Materials for Advanced Lithium-Ion Batteries," *J. Phys. Chem. C*, vol. 121, no. 47, pp. 26163–26171, Nov. 2017.

[37] F. Strauss *et al.*, "Rational Design of Quasi-Zero-Strain NCM Cathode Materials for Minimizing Volume Change Effects in All-Solid-State Batteries," *ACS Mater. Lett.*, vol. 2, no. 1, pp. 84–88, Jan. 2020.

[38] F. C. Strobridge *et al.*, "Unraveling the Complex Delithiation Mechanisms of Olivine-Type Cathode Materials, LiFe$_x$Co$_{1-x}$PO$_4$," *Chem. Mater.*, vol. 28, no. 11, pp. 3676–3690, Jun. 2016.

[39] G. G. Amatucci, J. M. Tarascon, and L. C. Klein, "CoO$_2$, the end member of the Li$_x$CoO$_2$ solid solution," *J. Electrochem. Soc.*, vol. 143, no. 3, pp. 1114–1123, 1996.

[40] X. L. Wang *et al.*, "Visualizing the chemistry and structure dynamics in lithium-ion batteries by in-situ neutron diffraction," *Sci. Rep.*, vol. 2, no. 1, pp. 1–7, Oct. 2012.

[41] A. O. Kondrakov *et al.*, "Charge-transfer-induced lattice collapse in Ni-rich NCM cathode materials during delithiation," *J. Phys. Chem. C*, vol. 121, no. 39, 2017.

[42] C. Zuo *et al.*, "Double the Capacity of Manganese Spinel for Lithium-Ion Storage by Suppression of Cooperative Jahn–Teller Distortion," *Adv. Energy Mater.*, vol. 10, no. 34, p. 2000363, Sep. 2020.

[43] Q. Xie, W. Li, and A. Manthiram, "A Mg-Doped High-Nickel Layered Oxide Cathode Enabling Safer, High-Energy-Density Li-Ion Batteries," *Chem. Mater.*, vol. 31, no. 3, pp. 938–946, Feb. 2019.

[44] T. Ohzuku and A. Ueda, "Solid-State Redox Reactions of $LiCoO_2$ (R3m) for 4 Volt Secondary Lithium Cells," *J. Electrochem. Soc.*, vol. 141, no. 11, pp. 2972–2977, 1994.

[45] J. N. Reimers and J. R. Dahn, "Electrochemical and in situ x-ray diffraction studies of lithium intercalation in Li_xCoO_2," *J. Electrochem. Soc.*, vol. 139, no. 8, pp. 2091–2097, 1992.

[46] M. Broussely *et al.*, "Main aging mechanisms in Li ion batteries," *J. Power Sources*, vol. 146, no. 1–2, pp. 90–96, 2005.

[47] W. M. Dose, J. K. Morzy, A. Mahadevegowda, C. Ducati, C. P. Grey, and M. F. L. De Volder, "The influence of electrochemical cycling protocols on capacity loss in nickel-rich lithium-ion batteries," *J. Mater. Chem. A*, vol. 9, no. 41, pp. 23582–23596, 2021.

[48] M. S. Whittingham, "Lithium batteries and cathode materials," *Chem. Rev.*, vol. 104, no. 10, pp. 4271–4301, 2004.

[49] M. M. Shaijumon, E. Perre, B. Daffos, P.-L. Taberna, J.-M. Tarascon, and P. Simon, "Nanoarchitectured 3D cathodes for Li-ion microbatteries," *Adv. Mater.*, vol. 22, no. 44, pp. 4978–4981, 2010.

[50] L. Chen *et al.*, "Hierarchical Li1.2Ni0.2Mn0.6O2 nanoplates with exposed {010} planes as high-performance cathode material for lithium-ion batteries," *Adv. Mater.*, vol. 26, no. 39, pp. 6756–6760, 2014.

[51] D. Y. Wang *et al.*, " A Systematic Study of Electrolyte Additives in Li[Ni 1/3 Mn 1/3 Co 1/3]O 2 (NMC)/Graphite Pouch Cells ," *J. Electrochem. Soc.*, vol. 161, no. 12, pp. A1818–A1827, 2014.

[52] K. Xu, "Nonaqueous liquid electrolytes for lithium-based rechargeable batteries," *Chem. Rev.*, vol. 104, no. 10, pp. 4303–4417, 2004.

[53] W. M. Dose, C. Xu, C. P. Grey, and M. F. L. De Volder, "Effect of Anode Slippage on Cathode Cutoff Potential and Degradation Mechanisms in Ni-Rich Li-Ion Batteries," *Cell Reports Phys. Sci.*, vol. 1, no. 11, 2020.

[54] J. M. Reniers, G. Mulder, and D. A. Howey, "Review and performance comparison of mechanical-chemical degradation models for lithium-ion batteries," *J. Electrochem. Soc.*, vol. 166, no. 14, pp. A3189–A3200, 2019.

[55] K. Zhao, M. Pharr, J. J. Vlassak, and Z. Suo, "Fracture of electrodes in lithium-ion batteries caused by fast charging," *J. Appl. Phys.*, vol. 108, no. 7, 2010.

[56] M. Zhu, J. Park, and A. M. Sastry, "Fracture analysis of the cathode in Li-ion batteries: A simulation study," *J. Electrochem. Soc.*, vol. 159, no. 4, 2012.

[57] R. Purkayastha and R. McMeeking, "A parameter study of intercalation of lithium into storage particles in a lithium-ion battery," *Comput. Mater. Sci.*, vol. 80, pp. 2–14, 2013.

[58] W. H. Woodford, Y.-M. Chiang, and W. C. Carter, "'Electrochemical shock' of intercalation electrodes: A fracture mechanics analysis," *J. Electrochem. Soc.*, vol. 157, no. 10, 2010.

[59] X. Zhang, W. Shyy, and A. Marie Sastry, "Numerical simulation of intercalation-induced stress in Li-Ion battery electrode Particles," *J. Electrochem. Soc.*, vol. 154, no. 10, 2007.

[60] J. Christensen and J. Newman, "Stress generation and fracture in lithium insertion materials," *J. Solid State Electrochem.*, vol. 10, no. 5, pp. 293–319, 2006.

[61] K. Dokko, M. Nishizawa, S. Horikoshi, T. Itoh, M. Mohamedi, and I. Uchida, "In situ observation of $LiNiO_2$ single-particle fracture during Li-Ion extraction and insertion," *Electrochem. Solid-State Lett.*, vol. 3, no. 3, pp. 125–127, 2000.

[62] R. Xu and K. Zhao, "Corrosive fracture of electrodes in Li-ion batteries," *J. Mech. Phys. Solids*, vol. 121, pp. 258–280, Dec. 2018.

[63] T. K. Bhandakkar and H. Gao, "Cohesive modeling of crack nucleation under diffusion induced stresses in a thin strip: Implications on the critical size for flaw tolerant battery electrodes," *Int. J. Solids Struct.*, vol. 47, no. 10, pp. 1424–1434, May 2010.

[64] Y. Hu, X. Zhao, and Z. Suo, "Averting cracks caused by Insertion reaction In lithium-ion batteries," *J. Mater. Res.*, vol. 25, no. 6, pp. 1007–1010, 2010.

[65] M. Qu, W. H. Woodford, J. M. Maloney, W. C. Carter, Y.-M. Chiang, and K. J. Van Vliet, "Nanomechanical quantification of elastic, plastic, and fracture properties of LiCoO2," *Adv. Energy Mater.*, vol. 2, no. 8, pp. 940–944, 2012.

[66] M. Z. Mughal, H.-Y. Amanieu, R. Moscatelli, and M. Sebastiani, "A comparison of microscale techniques for determining fracture toughness of $LiMn_2O_4$ particles," *Materials (Basel).*, vol. 10, no. 4, p. 403, 2017.

[67] J. Wolfenstine *et al.*, "$LiCoPO_4$ mechanical properties evaluated by nanoindentation," *Ceram. Int.*, vol. 40, no. 8 PART B, pp. 13673–13677, 2014.

[68] M. Z. Mughal, R. Moscatelli, H.-Y. Amanieu, and M. Sebastiani, "Effect of lithiation on micro-scale fracture toughness of $Li_xMn_2O_4$ cathode," *Scr. Mater.*, vol. 116, pp. 62–66, 2016.

[69] H.-Y. Amanieu, D. Rosato, M. Sebastiani, F. Massimi, and D. C. Lupascu, "Mechanical property measurements of heterogeneous materials by selective nanoindentation: Application to $LiMn_2O_4$ cathode," *Mater. Sci. Eng. A*, vol. 593, pp. 92–102, 2014.

[70] K. Zeng and J. Zhu, "Surface morphology, elastic modulus and hardness of thin film cathodes for Li-ion rechargeable batteries," *Mech. Mater.*, vol. 91, pp. 323–332, 2015.

[71] F. P. McGrogan, Y.-M. Chiang, and K. J. Van Vliet, "Effect of transition metal substitution on elastoplastic properties of $LiMn_2O_4$ spinel," *J. Electroceramics*, vol. 38,

no. 2–4, pp. 215–221, 2017.

[72] H.-Y. Amanieu, M. Aramfard, D. Rosato, L. Batista, U. Rabe, and D. C. Lupascu, "Mechanical properties of commercial $^{Li}xMn_2O_4$ cathode under different States of Charge," *Acta Mater.*, vol. 89, pp. 153–162, 2015.

[73] L. S. de Vasconcelos, N. Sharma, R. Xu, and K. Zhao, "In-Situ Nanoindentation Measurement of Local Mechanical Behavior of a Li-Ion Battery Cathode in Liquid Electrolyte," *Exp. Mech.*, vol. 59, no. 3, pp. 337–347, 2019.

[74] R. Xu, H. Sun, L. S. De Vasconcelos, and K. Zhao, "Mechanical and structural degradation of $LiNi_xMn_yCo_2O_2$ cathode in Li-ion batteries: An experimental study," *J. Electrochem. Soc.*, vol. 164, no. 13, pp. A3333–A3341, 2017.

[75] E. J. Cheng, K. Hong, N. J. Taylor, H. Choe, J. Wolfenstine, and J. Sakamoto, "Mechanical and physical properties of $LiNi_{0.33}Mn_{0.33}Co_{0.33}O_2$ (NMC)," *J. Eur. Ceram. Soc.*, vol. 37, no. 9, pp. 3213–3217, 2017.

[76] E. J. Cheng, N. J. Taylor, J. Wolfenstine, and J. Sakamoto, "Elastic properties of lithium cobalt oxide ($LiCoO_2$)," *J. Asian Ceram. Soc.*, vol. 5, no. 2, pp. 113–117, 2017.

[77] M. Sebastiani, K. E. Johanns, E. G. Herbert, F. Carassiti, and G. M. Pharr, "A novel pillar indentation splitting test for measuring fracture toughness of thin ceramic coatings," *Philos. Mag.*, vol. 95, no. 16–18, pp. 1928–1944, 2015.

[78] D. Tabor, *The hardness of metals.* Oxford: Oxford : Clarendon Press, 1951., 1951.

[79] M. F. Doerner and W. D. Nix, "A method for interpreting the data from depth-sensing indentation instruments," *J. Mater. Res.*, vol. 1, no. 4, pp. 601–609, 1986.

[80] G. M. Pharr, "Measurement of mechanical properties by ultra-low load indentation," *Mater. Sci. Eng. A*, vol. 253, no. 1–2, pp. 151–159, 1998.

[81] W. C. Oliver and G. M. Pharr, "Improved technique for determining hardness and elastic modulus using load and displacement sensing indentation experiments," *J. Mater. Res.*, vol. 7, no. 6, pp. 1564–1580, 1992.

[82] D. R. H. Jones and M. F. Ashby, *Engineering materials 1: An introduction to properties, applications and design*. 2019.

[83] M. F. Ashby and D. R. H. Jones, *Engineering Materials 2: An Introduction to Microstructures, Processing and Design: Second Edition*. 2013.

[84] G. M. Pharr, E. G. Herbert, and Y. Gao, *The indentation size effect: A critical examination of experimental observations and mechanistic interpretations*, vol. 40. 2010.

[85] I. Manika and J. Maniks, "Size effects in micro- and nanoscale indentation," *Acta Mater.*, vol. 54, no. 8, pp. 2049–2056, 2006.

[86] B. J. Hockey, "Plastic Deformation of Aluminum Oxide by Indentation and Abrasion," *J. Am. Ceram. Soc.*, vol. 54, no. 5, pp. 223–231, 1971.

[87] J. B. Pethica and D. Tabor, "Contact of characterised metal surfaces at very low loads:

Deformation and adhesion," *Surf. Sci.*, vol. 89, no. 1–3, pp. 182–190, 1979.

[88] N. A. Sakharova, J. V. Fernandes, J. M. Antunes, and M. C. Oliveira, "Comparison between Berkovich, Vickers and conical indentation tests: A three-dimensional numerical simulation study," *Int. J. Solids Struct.*, vol. 46, no. 5, pp. 1095–1104, 2009.

[89] M. F. Ashby and C. G. Sammis, "The damage mechanics of brittle solids in compression," *Pure Appl. Geophys. PAGEOPH*, vol. 133, no. 3, pp. 489–521, 1990.

[90] M. F. Ashby and S. D. Hallam (Née Cooksley), "The failure of brittle solids containing small cracks under compressive stress states," *Acta Metall.*, vol. 34, no. 3, pp. 497–510, 1986.

[91] V. S. Deshpande and A. G. Evans, "Inelastic deformation and energy dissipation in ceramics: A mechanism-based constitutive model," *J. Mech. Phys. Solids*, vol. 56, no. 10, pp. 3077–3100, 2008.

[92] V. S. Deshpande, E. A. N. Gamble, B. G. Compton, R. M. McMeeking, A. G. Evans, and F. W. Zok, "A constitutive description of the inelastic response of ceramics," *J. Am. Ceram. Soc.*, vol. 94, no. SUPPL. 1, pp. s204–s214, 2011.

[93] E. A. Gamble, B. G. Compton, V. S. Deshpande, A. G. Evans, and F. W. Zok, "Damage development in an armor ceramic under quasi-static indentation," *J. Am. Ceram. Soc.*, vol. 94, no. SUPPL. 1, pp. s215–s225, 2011.

[94] W. F. Brace, B. W. Paulding Jr., and C. Scholz, "Dilatancy in the fracture of crystalline rocks," *J. Geophys. Res.*, vol. 71, no. 16, pp. 3939–3953, Aug. 1966.

[95] W. F. Brace, "Volume changes during fracture and frictional sliding: A review," *Pure Appl. Geophys. PAGEOPH*, vol. 116, no. 4–5, pp. 603–614, 1978.

[96] F. Guiberteau, N. P. Padture, and B. R. Lawn, "Effect of Grain Size on Hertzian Contact Damage in Alumina," *J. Am. Ceram. Soc.*, vol. 77, no. 7, pp. 1825–1831, 1994.

[97] J. G. Swallow, W. H. Woodford, F. P. McGrogan, N. Ferralis, Y.-M. Chiang, and K. J. Van Vliet, "Effect of electrochemical charging on elastoplastic properties and fracture toughness of Li_xCoO_2," *J. Electrochem. Soc.*, vol. 161, no. 11, pp. f3084–f3090, 2014.

[98] G. I. Taylor, "The mechanism of plastic deformation of crystals. Part I.—Theoretical," *Proc. R. Soc. London. Ser. A, Contain. Pap. a Math. Phys. Character*, vol. 145, no. 855, pp. 362–387, Jul. 1934.

[99] N. A. Fleck, G. M. Muller, M. F. Ashby, and J. W. Hutchinson, "Strain gradient plasticity: Theory and experiment," *Acta Metall. Mater.*, vol. 42, no. 2, pp. 475–487, 1994.

[100] W. J. Poole, M. F. Ashby, and N. A. Fleck, "Micro-hardness of annealed and work-hardened copper polycrystals," *Scr. Mater.*, vol. 34, no. 4, pp. 559–564, 1996.

[101] Y. Fu and A. G. Evans, "Some effects of microcracks on the mechanical properties of brittle solids-I. Stress, strain relations," *Acta Metall.*, vol. 33, no. 8, pp. 1515–1523, 1985.

[102] B. Budiansky and R. J. O'connell, "Elastic moduli of a cracked solid," *Int. J. Solids*

Struct., vol. 12, no. 2, pp. 81–97, 1976.

[103] B. R. Lawn and M. V. Swain, "Microfracture beneath point indentations in brittle solids," *J. Mater. Sci.*, vol. 10, no. 1, pp. 113–122, 1975.

[104] B. R. Lawn and A. G. Evans, "A model for crack initiation in elastic/plastic indentation fields," *J. Mater. Sci.*, vol. 12, no. 11, pp. 2195–2199, 1977.

[105] G. R. Anstis, P. Chantikul, B. R. Lawn and D. B. Marshall, "A Critical Evaluation of Indentation Techniques for Measuring Fracture Toughness: I, Direct Crack Measurements," *J. Am. Ceram. Soc.*, vol. 64, no. 9, pp. 533–538, 1981.

[106] D. Dang, Y. Wang, and Y.-T. Cheng, "Communication — Fracture behavior of single $LiNi_{0.33}Co_{0.33}O_2$ particles studied by flat punch indentation," *J. Electrochem. Soc.*, vol. 166, no. 13, pp. A2749–A2751, 2019.

[107] Y. Hiramatsu and Y. Oka, "Determination of the tensile strength of rock by a compression test of an irregular test piece," *Int. J. Rock Mech. Min. Sci.*, vol. 3, no. 2, pp. 89–90, 1966.

[108] H. G., "The evaluation of Poisson's ratio and the modulus of materials of low tensile resistance by the Brazilian (Indirect tensile) test with particular reference to concrete," *Aust. J. Appl. Sci.*, vol. 10, no. 3, pp. 243–268, 1959.

[109] M. Yoshida, H. Ogiso, S. Nakano, and J. Akedo, "Compression test system for a single submicrometer particle," *Rev. Sci. Instrum.*, vol. 76, no. 9, 2005.

[110] W. Huddleston, F. Dynys, and A. Sehirlioglu, "Effects of microstructure on fracture strength and conductivity of sintered NMC333," *J. Am. Ceram. Soc.*, vol. 103, no. 3, pp. 1527–1535, 2020.

[111] C28 Committee, "Standard Test Method for Monotonic Equibiaxial Flexural Strength of Advanced Ceramics at Ambient Temperature," ASTM International, 2019.

[112] E04 Committee, "Standard Test Methods for Determining Average Grain Size," ASTM International, 2019.

[113] E. Orowan, "Fracture and strength of solids," *Reports Prog. Phys.*, vol. 12, no. 1, pp. 185–232, 1949.

[114] R. W. Rice, "Ceramic tensile strength-grain size relations: Grain sizes, slopes, and branch intersections," *J. Mater. Sci.*, vol. 32, no. 7, pp. 1673–1692, 1997.

[115] H. H. Ryu, K. J. Park, C. S. Yoon, and Y. K. Sun, "Capacity fading of ni-rich li[NixCoyMn1-x-y]O2 (0.6 ≤ x ≤ 0.95) Cathodes for High-Energy-Density Lithium-Ion Batteries: Bulk or Surface Degradation?," *Chem. Mater.*, vol. 30, no. 3, pp. 1155–1163, Feb. 2018.

[116] R. Xu, H. Sun, L. S. de Vasconcelos, and K. Zhao, "Mechanical and Structural Degradation of $LiNi_xMn_yCo_zO_2$ Cathode in Li-Ion Batteries: An Experimental Study," *J. Electrochem. Soc.*, vol. 164, no. 13, pp. A3333–A3341, Nov. 2017.

[117] R. Ruess *et al.*, "Influence of NCM Particle Cracking on Kinetics of Lithium-Ion Batteries with Liquid or Solid Electrolyte," *J. Electrochem. Soc.*, vol. 167, no. 10, 2020.

[118] I. Soroka and P. J. Sereda, "Interrelation of Hardness, Modulus of Elasticity, and Porosity in Various Gypsum Systems," *J. Am. Ceram. Soc.*, vol. 51, no. 6, pp. 337–340, 1968.

[119] R. L. Coble and W. D. Kingery, "Effect of Porosity on Physical Properties of Sintered Alumina," *J. Am. Ceram. Soc.*, vol. 39, no. 11, pp. 377–385, 1956.

[120] D. C. C. Lam, F. F. Lange, and A. G. Evans, "Mechanical Properties of Partially Dense Alumina Produced from Powder Compacts," *J. Am. Ceram. Soc.*, vol. 77, no. 8, pp. 2113–2117, 1994.

[121] T. M. M. Heenan *et al.*, "Identifying the Origins of Microstructural Defects Such as Cracking within Ni-Rich NMC811 Cathode Particles for Lithium-Ion Batteries," *Adv. Energy Mater.*, vol. 10, no. 47, p. 2002655, Dec. 2020.

[122] K. K. Phani and S. K. Niyogi, "Young's modulus of porous brittle solids," *J. Mater. Sci.*, vol. 22, no. 1, pp. 257–263, 1987.

[123] G.-L. Xu, X. Liu, A. Daali, R. Amine, Z. Chen, and K. Amine, "Challenges and Strategies to Advance High-Energy Nickel-Rich Layered Lithium Transition Metal Oxide Cathodes for Harsh Operation," *Adv. Funct. Mater.*, vol. 30, no. 46, 2020.

[124] A. Mukhopadhyay and B. W. Sheldon, "Deformation and stress in electrode materials for Li-ion batteries," *Prog. Mater. Sci.*, vol. 63, pp. 58–116, 2014.

[125] T. Li, X.-Z. Yuan, L. Zhang, D. Song, K. Shi, and C. Bock, "Degradation Mechanisms and Mitigation Strategies of Nickel-Rich NMC-Based Lithium-Ion Batteries," *Electrochem. Energy Rev.*, vol. 3, no. 1, pp. 43–80, Mar. 2020.

[126] H. H. Sun *et al.*, "Beyond Doping and Coating: Prospective Strategies for Stable High-Capacity Layered Ni-Rich Cathodes," *ACS Energy Lett.*, vol. 5, no. 4, pp. 1136–1146, 2020.

[127] Y. Mao *et al.*, "High-Voltage Charging-Induced Strain, Heterogeneity, and Micro-Cracks in Secondary Particles of a Nickel-Rich Layered Cathode Material," *Adv. Funct. Mater.*, vol. 29, no. 18, p. 1900247, May 2019.

[128] H. Li, P. Zhou, F. Liu, H. Li, F. Cheng, and J. Chen, "Stabilizing nickel-rich layered oxide cathodes by magnesium doping for rechargeable lithium-ion batteries," *Chem. Sci.*, vol. 10, no. 5, pp. 1374–1379, 2019.

[129] H. H. Sun *et al.*, "Transition metal-doped Ni-rich layered cathode materials for durable Li-ion batteries," *Nat. Commun.*, vol. 12, no. 1, 2021.

[130] Y.-K. Sun, S.-T. Myung, B.-C. Park, J. Prakash, I. Belharouak, and K. Amine, "High-energy cathode material for long-life and safe lithium batteries," *Nat. Mater.*, vol. 8, no. 4, pp. 320–324, 2009.

[131] U.-H. Kim, S.-T. Myung, C. S. Yoon, and Y.-K. Sun, "Extending the Battery Life Using an Al-Doped Li[Ni$_{0.76}$Co$_{0.09}$Mn$_{0.15}$]O$_2$ Cathode with Concentration Gradients for Lithium Ion Batteries," *ACS Energy Lett.*, vol. 2, no. 8, pp. 1848–1854, 2017.

[132] J. Li, R. Shunmugasundaram, R. Doig, and J. R. Dahn, "In Situ X-ray Diffraction Study of

Layered Li–Ni–Mn–Co Oxides: Effect of Particle Size and Structural Stability of Core–Shell Materials," *Chem. Mater.*, vol. 28, no. 1, pp. 162–171, Jan. 2016.

[133] H. Tanriöver and B. W. Sheldon, "The impact of compositionally induced residual stress on electrochemical shock in battery electrode particles," *J. Electrochem. Soc.*, vol. 162, no. 7, pp. A1282–A1288, 2015.

[134] H. Ryu, K. Park, D. R. Yoon, A. Aishova, C. S. Yoon, and Y. Sun, "Li[Ni$_{0.9}$ Co$_{0.09}$ W$_{0.01}$]O$_2$: A New Type of Layered Oxide Cathode with High Cycling Stability," *Adv. Energy Mater.*, vol. 9, no. 44, p. 1902698, Nov. 2019.

[135] G.-T. Park *et al.*, "Ultrafine-grained Ni-rich layered cathode for advanced Li-ion batteries," *Energy Environ. Sci.*, vol. 14, no. 12, pp. 6616–6626, 2021.

[136] X. Xu *et al.*, "Radially Oriented Single-Crystal Primary Nanosheets Enable Ultrahigh Rate and Cycling Properties of LiNi$_{0.8}$Co$_{0.1}$Mn$_{0.1}$O$_2$ Cathode Material for Lithium-Ion Batteries," *Adv. Energy Mater.*, vol. 9, no. 15, 2019.

[137] G. Qian *et al.*, "Single-crystal nickel-rich layered-oxide battery cathode materials: synthesis, electrochemistry, and intra-granular fracture," *Energy Storage Mater.*, vol. 27, pp. 140–149, 2020.

[138] J. Li *et al.*, "Comparison of single crystal and polycrystalline LiNi$_{0.5}$Mn$_{0.3}$Co$_{0.2}$O$_2$ positive electrode materials for high voltage Li-ion cells," *J. Electrochem. Soc.*, vol. 164, no. 7, pp. A1534–A1544, 2017.

[139] J. E. Harlow *et al.*, "A Wide Range of Testing Results on an Excellent Lithium-Ion Cell Chemistry to be used as Benchmarks for New Battery Technologies," *J. Electrochem. Soc.*, vol. 166, no. 13, pp. A3031–A3044, 2019.

[140] J. Li, H. Li, W. Stone, R. Weber, S. Hy, and J. R. Dahn, "Synthesis of single crystal LiNi$_{0.5}$Mn$_{0.3}$Co$_{0.2}$O$_2$ for lithium ion batteries," *J. Electrochem. Soc.*, vol. 164, no. 14, pp. A3529–A3537, 2017.

Figures

(a)
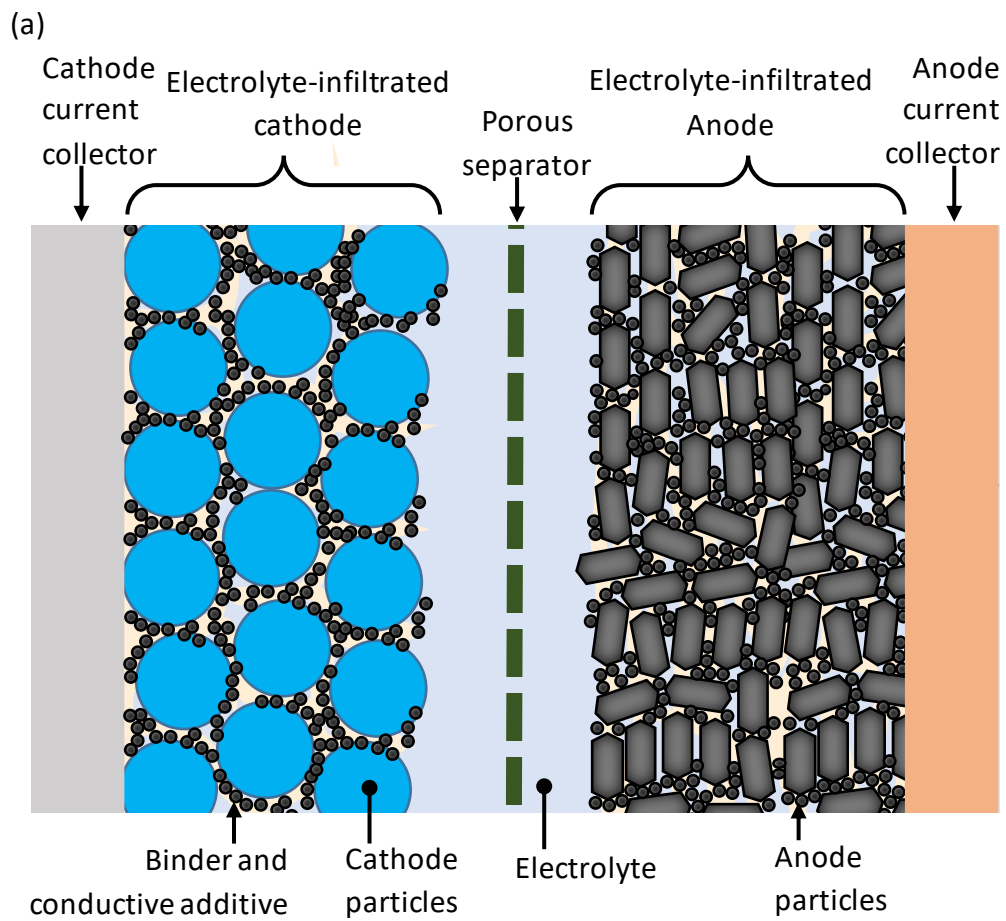
Figure 1: The structure of a Li-ion cell, illustrating the typical porous cathode microstructure of active particles bonded together with a conductive binder.
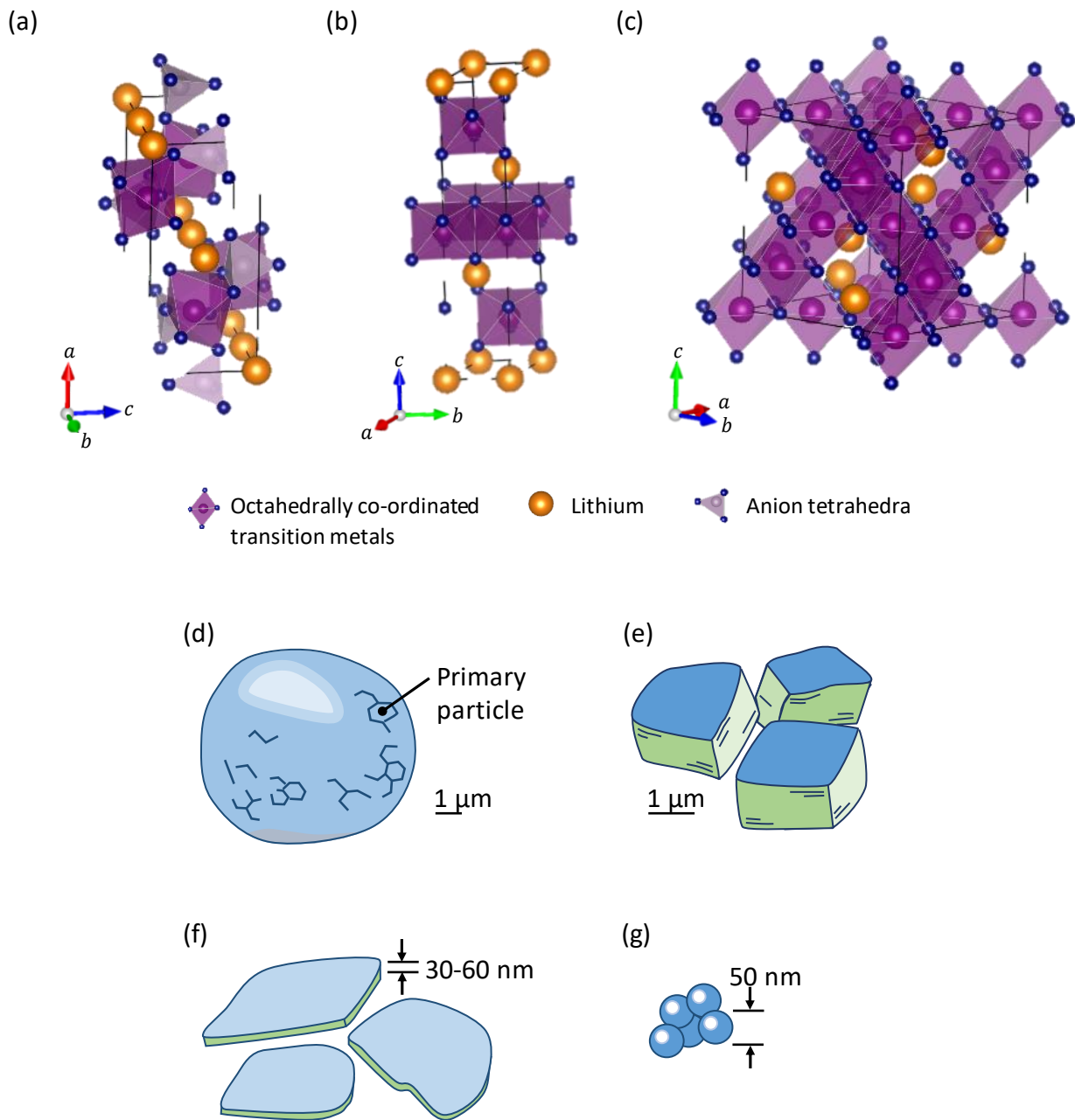
(a)

(b)

(c)

a c b

c b a

c a b

Octahedrally co-ordinated transition metals

Lithium

Anion tetrahedra

(d)

Primary particle

1 µm

(e)

1 µm

(f)

30-60 nm

(g)

50 nm

Figure 2: Typical atomic structures of (a) olivine, (b) layered and (c) spinel cathode materials. Sketches of different cathode particle architectures: (d) secondary particle, (e) separate single crystals [140], (f) plate-shaped particles [20], and (g) nano-sized particles [21].
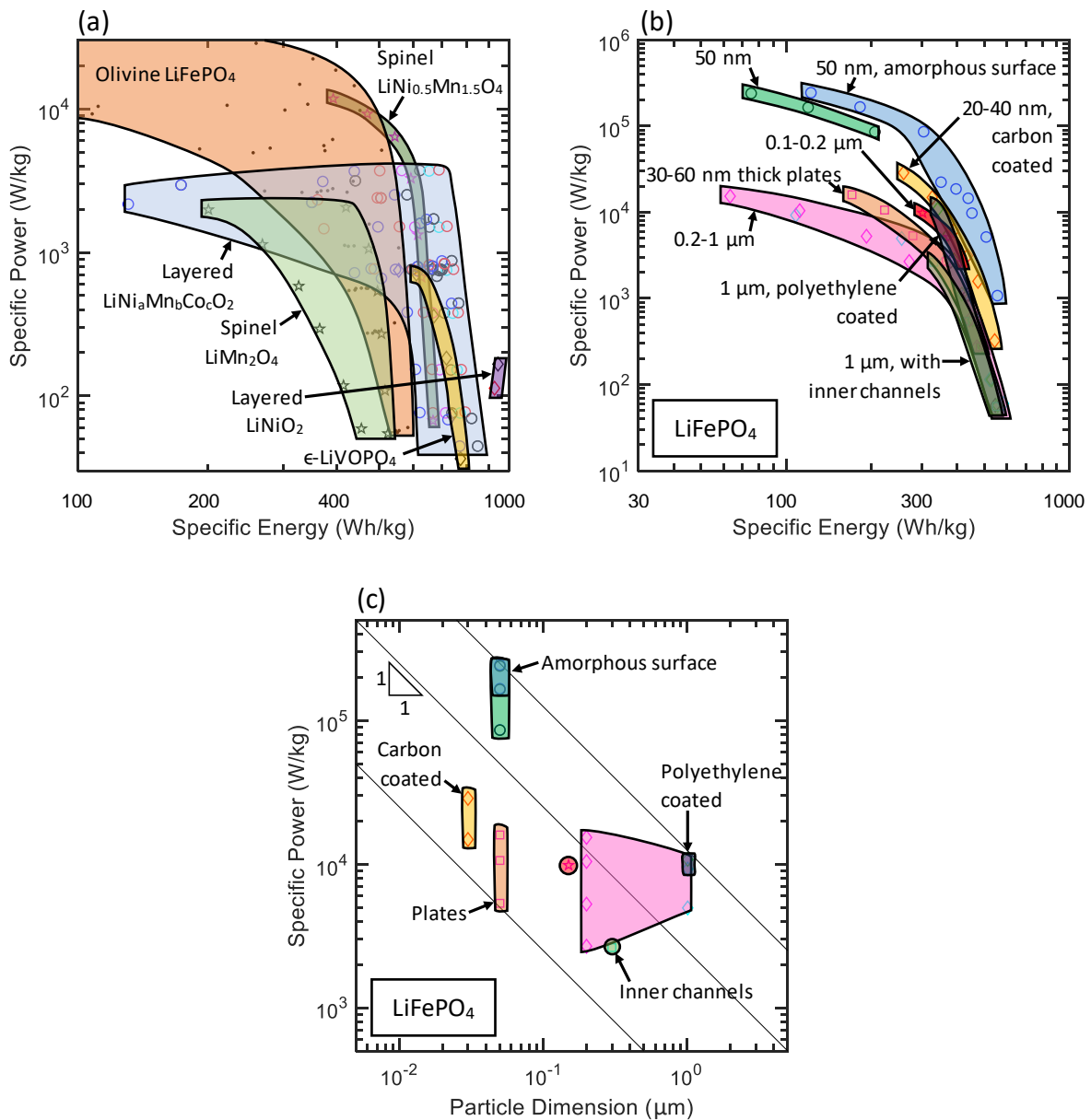
Figure 3: Plots of the specific power versus specific energy for (a) different cathode materials as reported in the literature [11], [19]–[29], (b) of LFP cathodes with a variety of different cathode particle architectures [11], [20]–[22], [27]–[29]. (c) The specific power of LFP cathodes versus particle dimension, for specific energy below 350 Wh kg^{-1}.
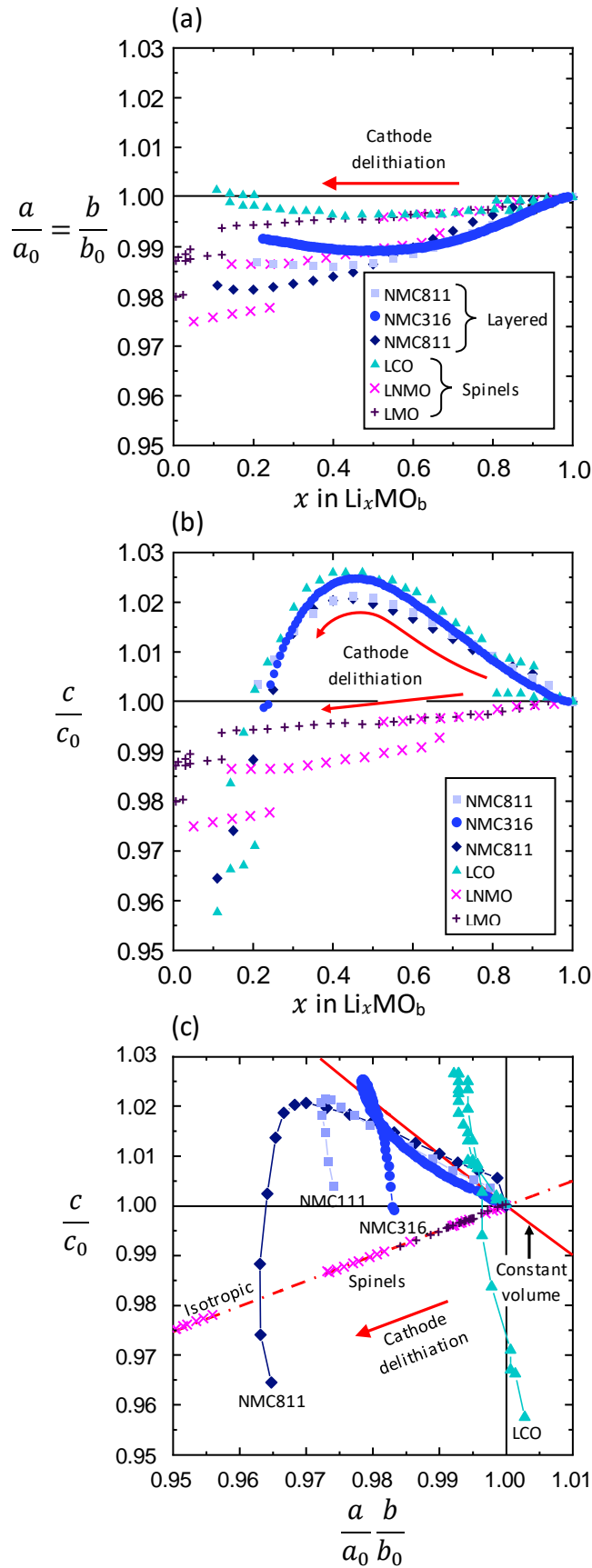
Figure 4: Normalised lattice constants (a) $a/a_0 = b/b_0$ and (b) c/c_0 plotted against degree of lithiation x in Li$_x$MO$_b$ as measured for a variety of layered and spinel cathode materials over the first cell charge [36]–[42] (c) Plot of c/c_0 versus $ab/(a_0 b_0)$.

37
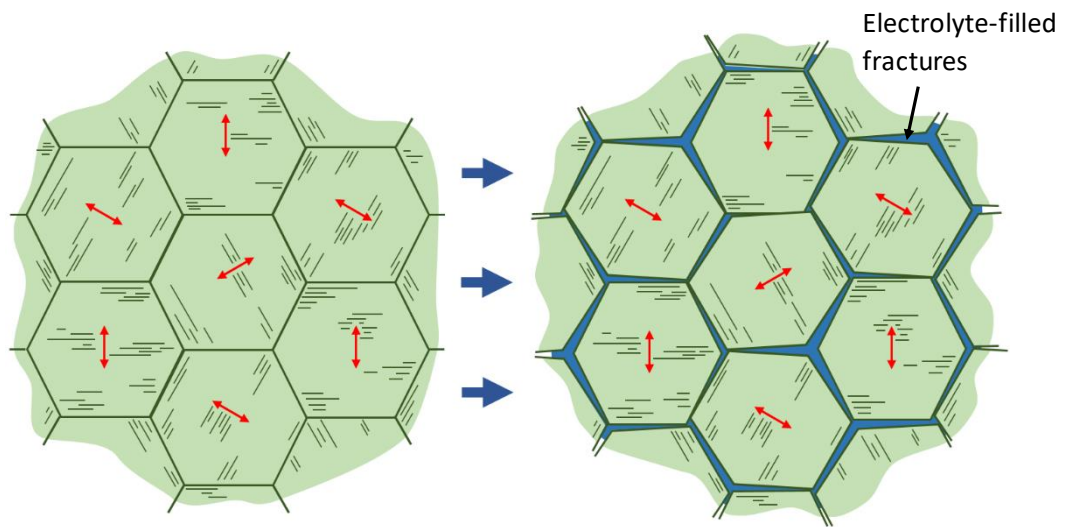
Figure 5: Sketch of the intergranular fracture that results from the anisotropic straining of layered cathode materials when in polycrystalline secondary particles. The arrows in each grain denote the direction of the c-axis.
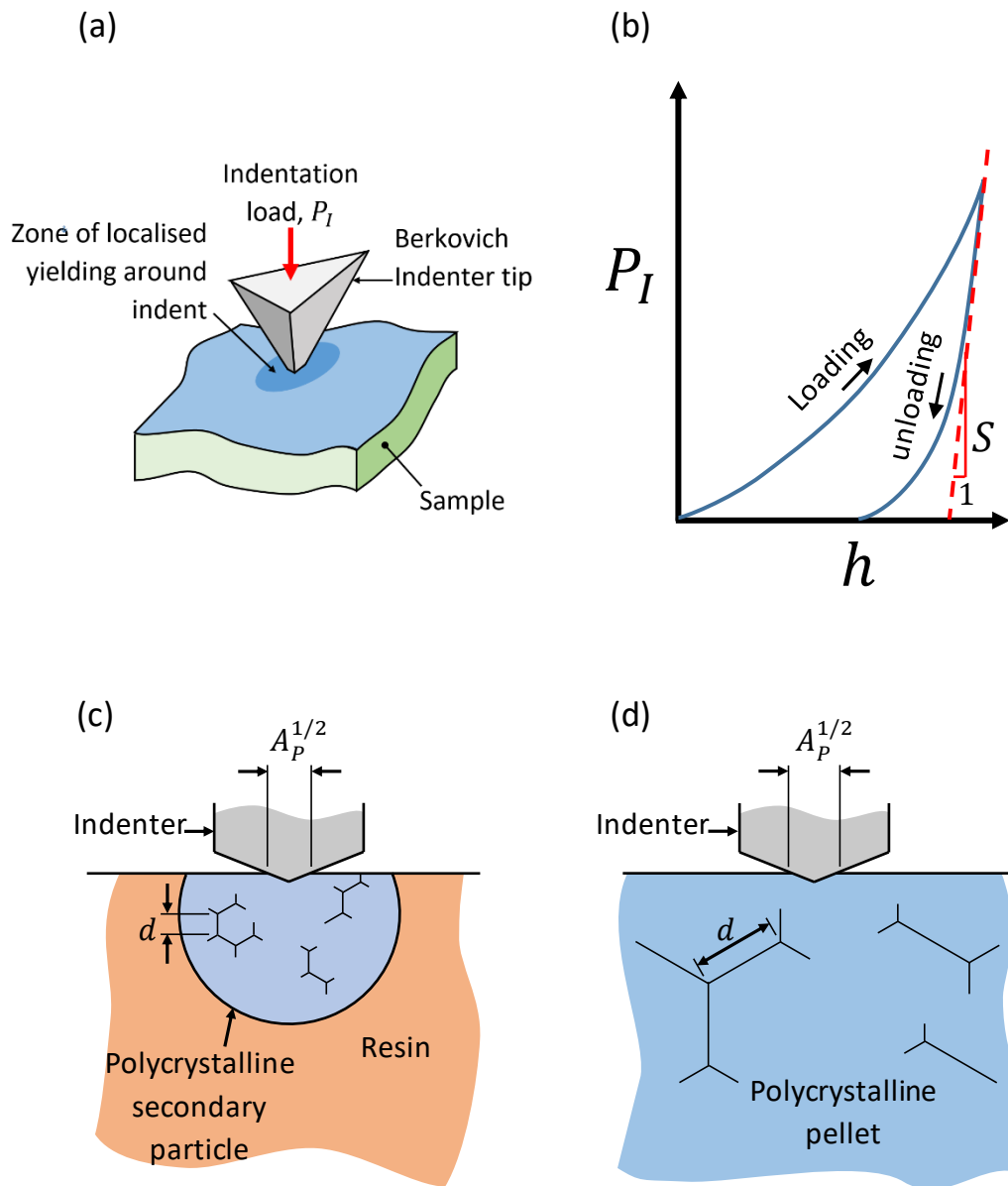
Figure 6: (a) Sketch of the indentation method used to measure hardness and modulus. (b) Sketch of a typical force-displacement response measured in indentation; the gradient used to deduce the Young's modulus from the elastic unloading response is identified. Sketch of the indentation of (c) secondary particle set in resin, and (d) a polycrystalline pellet of macroscopic dimensions. Note the differences in the ratio of indent size $A_P^{1/2}$ to grain size d.
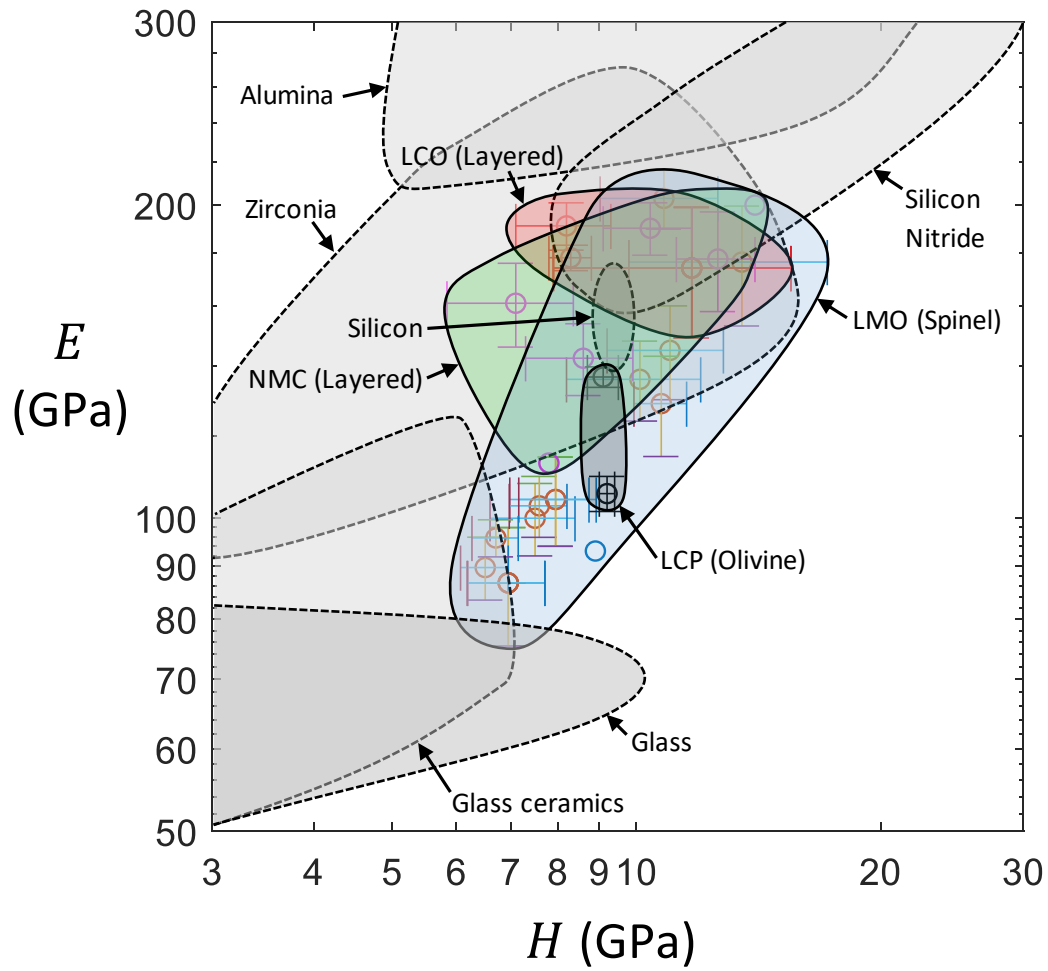
Figure 7: The modulus and hardness of a variety of cathode materials as measured after manufacture in the fully-lithiated state with Berkovich indentation [65]–[76] and compared against the modulus and hardness of other engineering ceramics and glasses [82], [83].
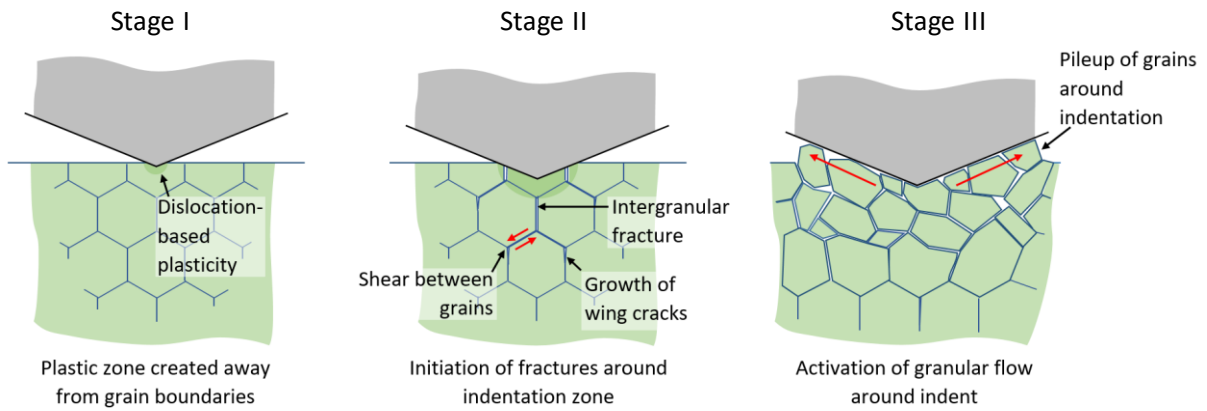
Figure 8: The idealised stages I, II and III of micromechanical deformation upon the indentation of a polycrystalline ceramic that give rise to decreasing hardness with increasing indentation area for indentations of dimension comparable to the grain size.
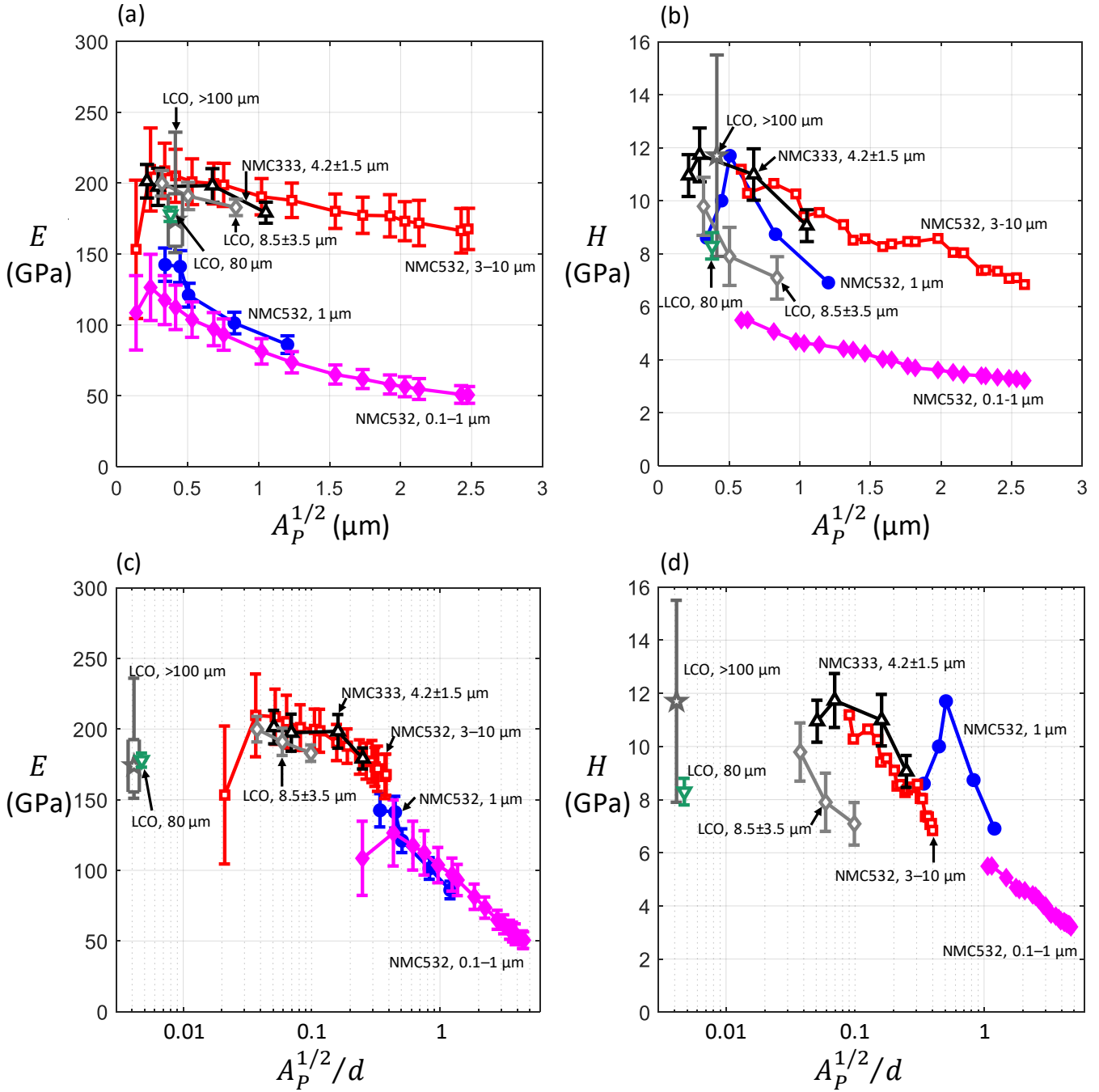
Figure 9: Young's modulus (a) and indentation hardness (b) plotted as a function of indentation size $A_I^{1/2}$ for a range of polycrystalline $LiNi_{0.5}Mn_{0.3}Co_{0.2}O_2$ and $LiNi_{1/3}Mn_{1/3}Co_{1/3}O_2$ cathode materials [65], [73]–[76], [97]. The modulus and hardness are plotted in figures (c) and (d), with the indentation size $A^{1/2}$ normalised by the grain size d. Data from secondary particles are indicated with filled symbols (●, ◆); data from sintered pellets are plotted with hollow symbols (△, ▽, ◇, ☆, □).
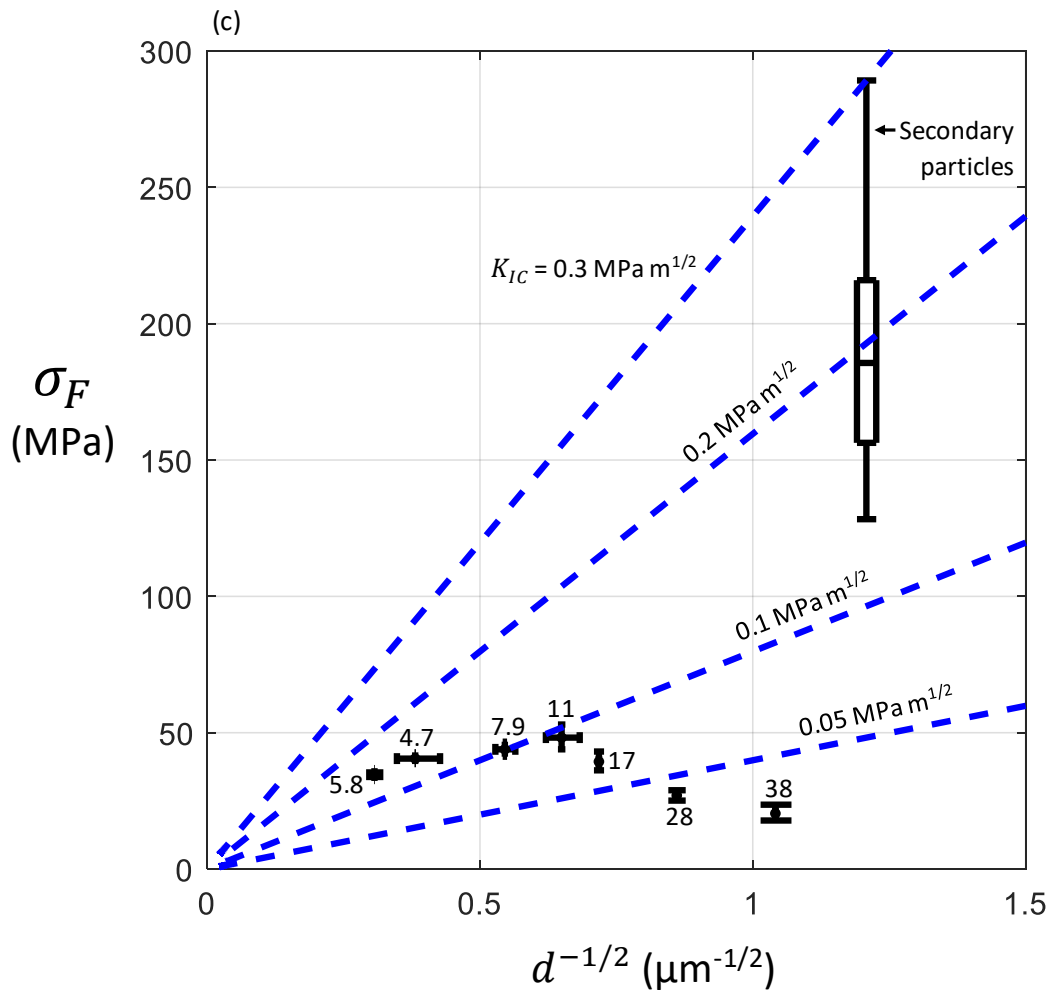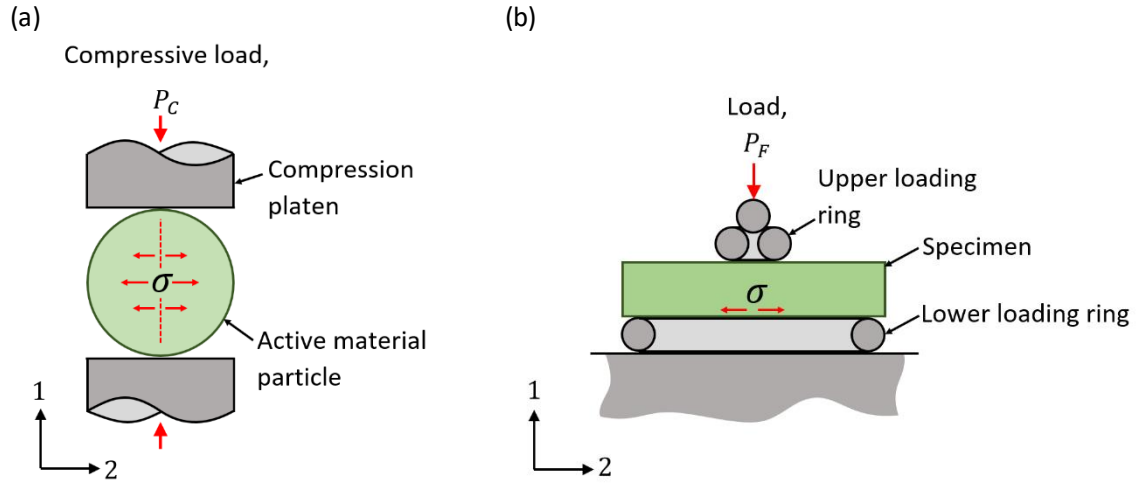
Figure 10: Methods of measuring the fracture strength of cathode materials: (a) the compression of secondary particles which leads to transverse tensile stress, (b) flexural bend tests on macroscopic cylindrical samples. (c) Plot of fracture strength σ_F versus $d^{-1/2}$ for NMC333 samples [106], [110]. Predictions of the fracture strength are included as contours for various values of fracture toughness, K_{IC}; the measured percentage of sample porosity are written alongside the data where available.
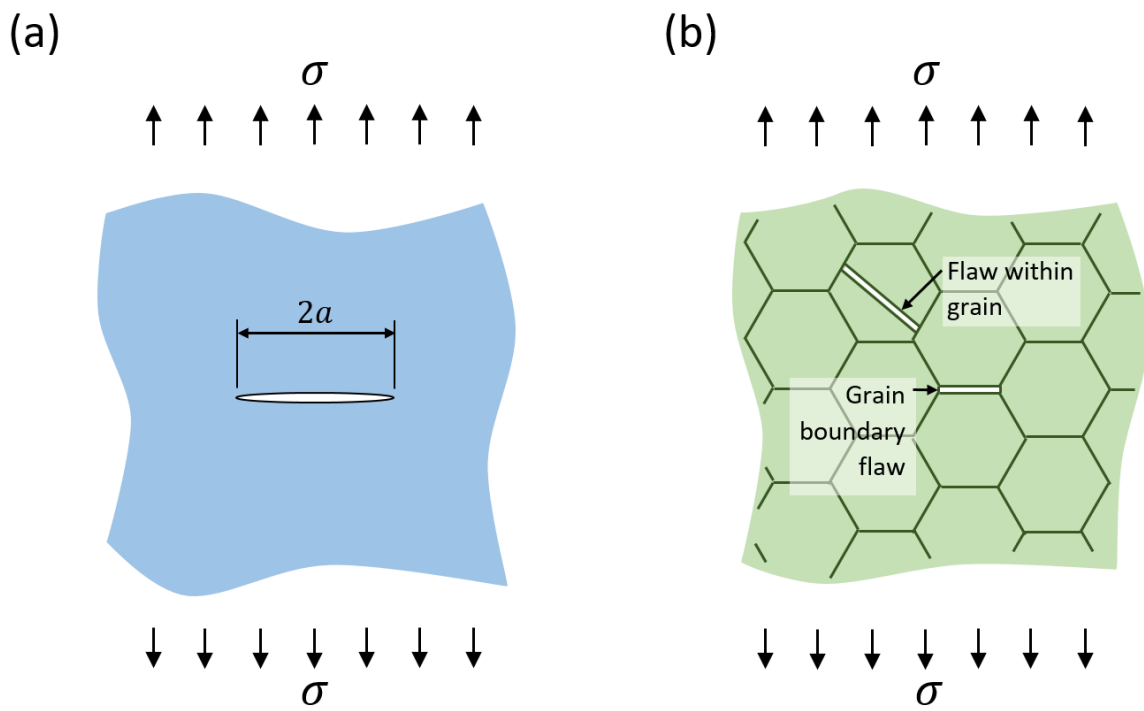
Figure 11: (a) Geometry of a flaw within a brittle material subjected to macroscopic stress, (b) typical flaws within a polycrystalline material of similar size to individual grains.
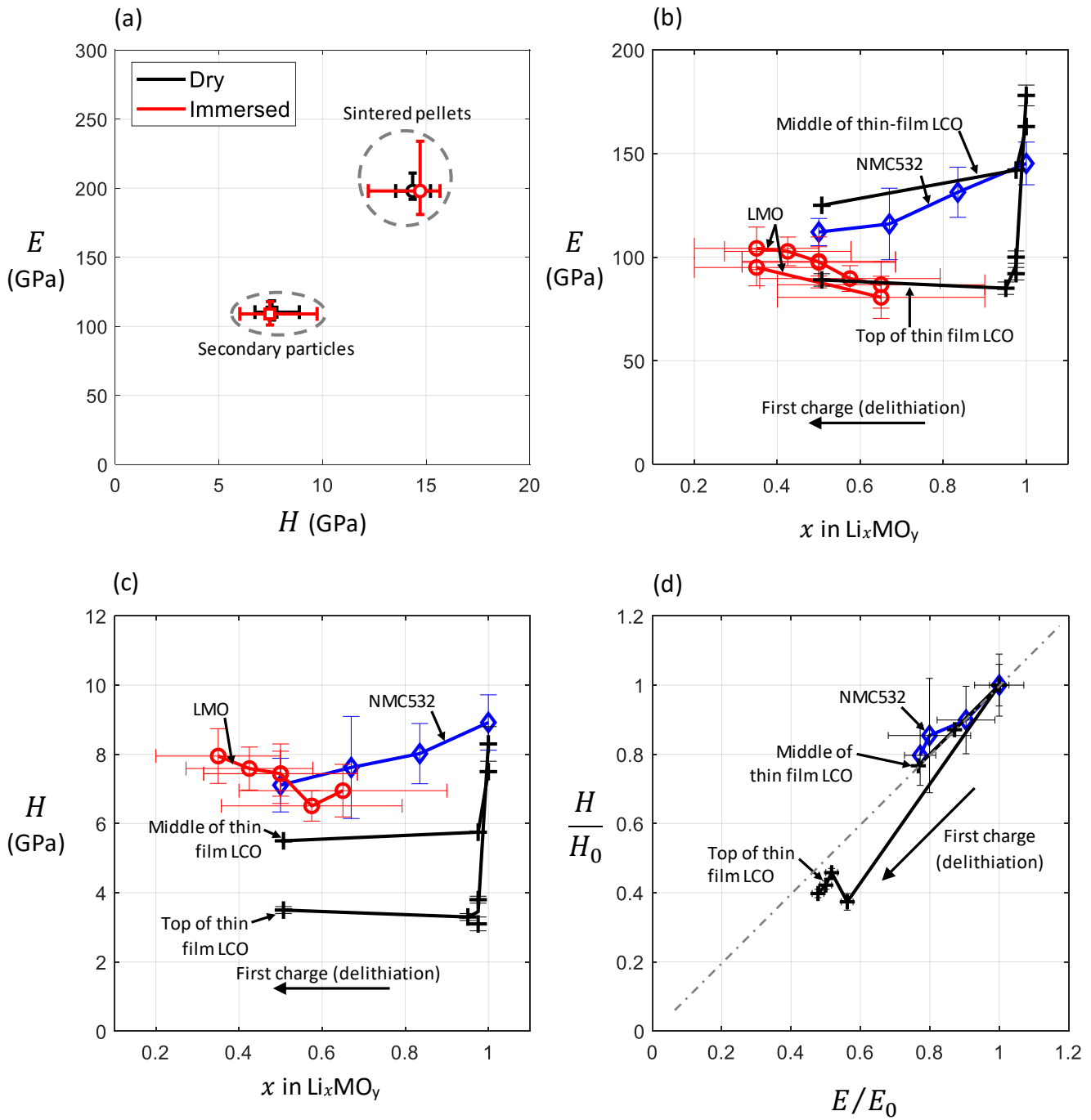
Figure 12: (a) the effect of electrolyte immersion upon the modulus E and hardness H of sintered pellets and secondary particles of NMC532. The (b) Young's modulus E and (c) indentation hardness H of cathode materials as a function of their degree of lithiation x over the first cell charge [68], [72], [97], [116]. The hardness H and modulus E of layered cathode materials are normalised by their values in a fully lithiated state, H_0 and E_0, and plotted against one another in (d).
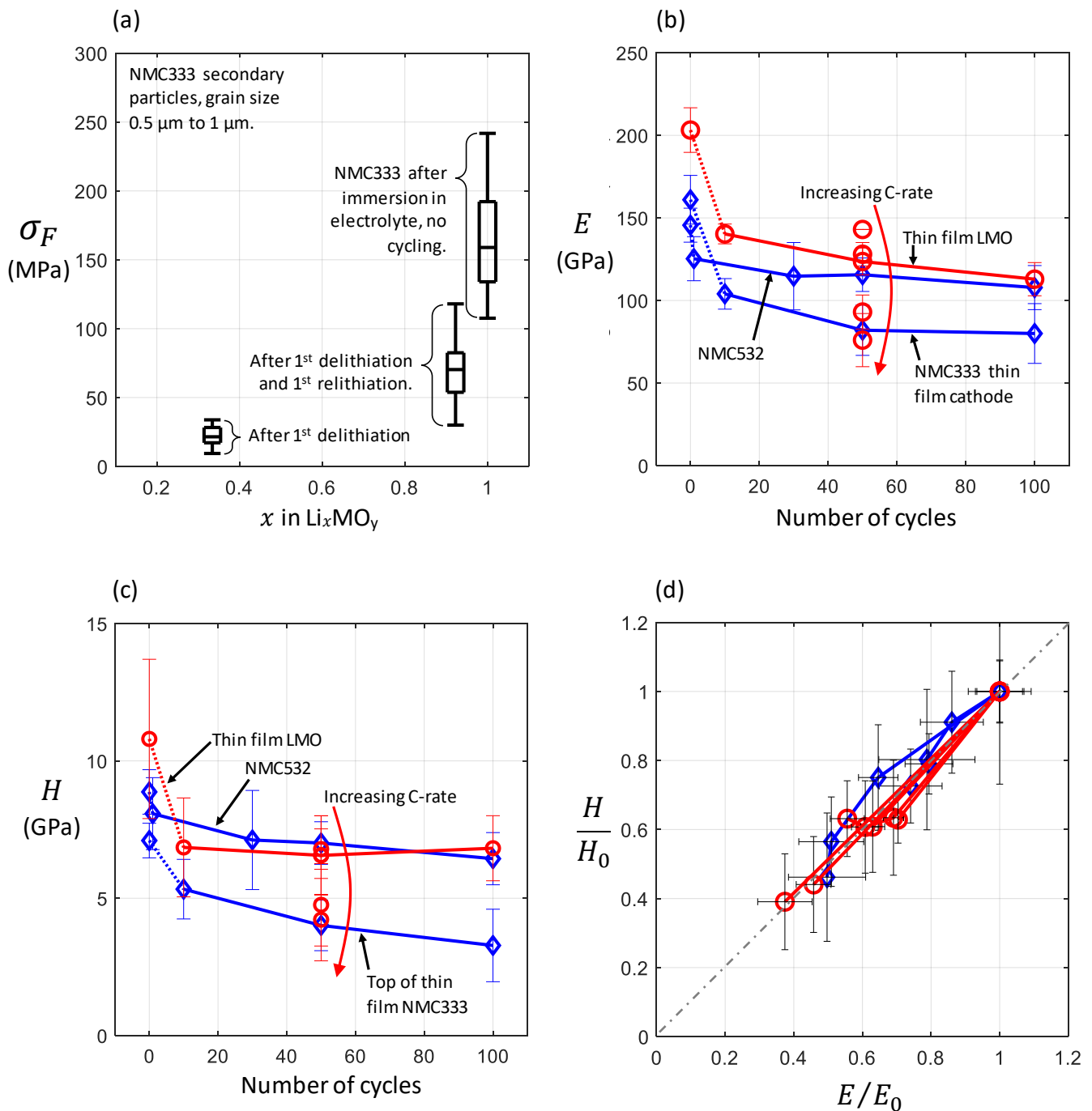
Figure 13: The effect of cycling upon mechanical properties [70], [74], [106]. (a) Effect of the first delithiation/relithiation cycle upon fracture strength σ_F for layered $Li_x Ni_{1/3} Mn_{1/3} Co_{1/3} O_2$. (b) Young's modulus E, and (c) hardness H of cathode materials as a function of the number of applied charge/discharge cycles, as measured in the lithiated state. Dotted lines are used where data span the first charge/discharge cycle, where the decrease in E and H is typically greatest. The hardness H and modulus E of layered cathode materials measured after successive charge/discharge cycles are normalised by their values before cycling, H_0 and E_0, and plotted against one another in (d).